

Helical-wave decomposition and applications to channel turbulence with streamwise rotation

Y.-T. YANG[†], W.-D. SU AND J.-Z. WU

State Key Laboratory of Turbulence and Complex Systems, College of Engineering,
Peking University, Beijing 100871, China

(Received 29 September 2009; revised 3 June 2010; accepted 3 June 2010;
first published online 5 August 2010)

Using helical-wave decomposition (HWD), a solenoidal vector field can be decomposed into helical modes with different wavenumbers and polarities. Here, we first review the general formulation of HWD in an arbitrary single-connected domain, along with some new development. We then apply the theory to a viscous incompressible turbulent channel flow with system rotation, including a derivation of helical bases for a channel domain. By these helical bases, we construct the inviscid inertial-wave (IW) solutions in a rotating channel and derive their existing condition. The condition determines the specific wavenumber and polarity of the IW. For a set of channel turbulent flows rotating about a streamwise axis, this channel-domain HWD is used to decompose the flow data obtained by direct numerical simulation. The numerical results indicate that the streamwise rotation induces a polarity-asymmetry and concentrates the fluctuating energy to particular helical modes. At large rotation rates, the energy spectra of opposite polarities exhibit different scaling laws. The nonlinear energy transfer between different helical modes is also discussed. Further investigation reveals that the IWs do exist when the streamwise rotation is strong enough, for which the theoretical predictions and numerical results are in perfect agreement in the core region. The wavenumber and polarity of the IW coincide with that of the most energetic helical modes in the energy spectra. The flow visualizations show that away from the channel walls, the small vortical structures are clustered to form very long columns, which move in the wall-parallel plane and serve as the carrier of the IW. These discoveries also help clarify certain puzzling problems raised in previous studies of streamwise-rotating channel turbulence.

Key words: rotating turbulence, turbulence simulation, turbulence theory

1. Introduction

System rotation is a frequently encountered circumstance in geophysical and engineering flows, such as large-scale atmospheric and oceanic flows and turbo-machinery flows. Rotating flow has long been an important branch of fluid dynamics (e.g. Phillips 1963; Greenspan 1969). Among various model-flow problems in the studies of rotating turbulence, rotating channel and pipe have been good vehicles since they are relatively easy to manufacture in experiment or simulate by numerical methods, and yet still may provide insights into wall-bounded rotating turbulence.

[†] Email address for correspondence: yytmech@pku.edu.cn

Early studies of the rotating-channel turbulence mainly focused on the spanwise rotation, i.e. the rotating axis parallel to the channel wall and perpendicular to the direction of the mean pressure gradient, such as the experiments by Johnston, Halleen & Lezius (1972) and Nakabayashi & Kitoh (1996, 2005), and the direct numerical simulations (DNS) by Kristoffersen & Andersson (1993) and Grundestam, Wallin & Johansson (2008). Recently, channel turbulence with streamwise rotation was investigated by several groups. Wu & Kasagi (2004) conducted the DNS of the channel flow with arbitrary directional rotation. Oberlack *et al.* (2006) used group analysis to study the streamwise-rotating channel theoretically, and validated the theory by DNS and turbulent model computation including Reynolds-averaged modelling and large-eddy simulation (LES). One major observation of these studies is the appearance of a secondary mean flow in the spanwise direction, which is zero at the centreline and antisymmetric about it. When observed against the rotating axis, the secondary mean flow is in the same direction as the rotation near the walls but in the opposite direction in the central region. The latter is referred to as the reverse mean flow in the spanwise direction. Similar secondary flow has also been found by Masuda, Fukuda & Nagata (2008) in a stability analysis of the plane Poiseuille flow at very low Reynolds number.

The same features of streamwise-rotating channel turbulence have been further studied by Recktenwald *et al.* (2007) by both experiment and DNS. The streamwise two-point correlations in their numerical results revealed that at the centre region of the channel there exist structures with very large streamwise scale. These long structures also exist in the streamwise-rotating pipe (see Orlandi & Fatica 1997). In the experiments of Recktenwald *et al.* (2007), however, no distinct reverse flow was found in the spanwise direction at the channel centre. Later, Alkishriwi, Meinke & Schröder (2008) and Recktenwald, Alkishriwi & Schröder (2009) conducted LES for streamwise-rotating channel with much larger computational box and different boundary conditions in the spanwise direction. The results show that in the LES with a larger domain the reverse mean flow is weaker than the DNS results, and was further reduced by introducing the no-slip endwalls in the spanwise direction. But the reverse mean flow, not seen in experiment, still existed in all these simulations. Nevertheless, one common understanding of the reverse spanwise flow at the channel centre is that it is related to the structures with large streamwise scales (e.g. see Recktenwald *et al.* 2007; Alkishriwi *et al.* 2008).

So far most research on the above problem has been confined to the physical space. In this study, we introduce the so-called helical-wave decomposition (HWD) to the channel turbulence with system rotation. For an arbitrary simple domain, the HWD decomposes a solenoidal vector field, such as velocity and vorticity of incompressible flows, into helical modes with different wavenumbers and opposite polarities. In our view, the polarities of a solenoidal vector field represent its two intrinsic independent components or degrees of freedom. Thus, HWD is a natural way to examine the respective physical role of each component and the coupling of multi-scales and opposite polarities. In fact, only a combined use of the Helmholtz–Hodge decomposition (HHD) and HWD can split a vector field into its finest intrinsic building blocks (see Wu, Ma & Zhou 2006). In many flows, although there is no predominance of a specific polarity, by introducing the polarity we may obtain new insights into the flow physics. Moreover, in some flows the polarity-symmetry may be broken. One example is the flow with system rotation, as we will discuss below.

This point of view has been supported by the previous discoveries of some innovative features by applying HWD to complex vortical flows and turbulence. In a

study of energy cascades for homogeneous turbulence, Waleffe (1992) has used HWD to investigate the triad interactions of helical modes and found that the polarities affect the direction of the energy transfer in each triad. Ditlevsen & Giuliani (2001*a,b*) utilized HWD to study the joint cascade of energy and helicity. Later, Chen, Chen & Eyink (2003) re-examined the same problem and proved that the nonlinear transfer between two opposite polarities permits the joint cascade. By studying the polarity property of flow structures, Hussain and co-workers found that the background fine-scale turbulence induces highly polarized and organized secondary structures near the coherent vortex (see Melander & Hussain 1993*a,b*).

HWD has already exhibited great advantages in the study of the rotating homogeneous turbulence. By studying the resonant-triad interactions and introducing an instability assumption, Waleffe (1993) showed that the flow has a tendency towards nonlinear two-dimensionalization, namely in each resonant triad the energy tends to be transferred to the wavenumber vectors whose angles with the rotating axis are closer to 90° . However, the author also proved that via the resonant triads there is no direct energy transfer between the strictly two-dimensional modes and the non-zero-frequency inertial-wave (IW) modes. For the moderate rotation rate, Smith & Lee (2005) verified numerically that the near-resonant-triad interactions dominate the energy transfer to the two-dimensional modes. The DNS results of Chen *et al.* (2005) showed the decoupling between the two-dimensional modes and the three-dimensional modes for moderate and relatively high rotation rates, which is consistent with the theoretical prediction of Waleffe (1993). Using equilibrium statistical mechanics at even higher rotation rates, this decoupling mechanism was also verified by Bourouiba (2008) until a certain time scale. Smith & Waleffe (1999) and Bourouiba & Bartello (2007) also observed the generation of the energetic two-dimensional modes in forced and decay rotating turbulent flows, respectively. Meanwhile, the HWD theory has been used to develop the closure model of rapidly rotating fluid by Cambon's group (see Bellet *et al.* 2006, and the reference therein).

A unique feature of the helical modes is that they can form the IW in a rotating fluid, as addressed by Greenspan (1969). The IW have been detected in the rotating tank by Bewley *et al.* (2007) and the spherical Couette flow by Kelley *et al.* (2010). The linear propagation of the IW provided an alternative explanation for the formation of the long columnar vortices in the experiments of the rotating homogeneous turbulence conducted by Davidson, Staplehurst & Dalziel (2006).

Despite the suitability of HWD to rotating turbulence and much research on the periodic domain, only a few studies have applied HWD to bounded domains. Nevertheless, Yoshida & Giga (1990) have laid the mathematical foundations for the application of HWD to an arbitrary domain. Chen *et al.* (2003) mentioned that their theory can be applied to a wall-bounded domain, but their numerical investigations were all in the periodic box. The HWD expansion has been used to simulate the magnetohydrodynamic activity in a rotating sphere by Shan & Montgomery (1994), Mininni & Montgomery (2006) and Mininni, Montgomery & Turner (2007). Recently, Ulitsky, Clark & Turner (1999) simulated channel flow with free-slip walls by HWD method, by which they aimed to test the random phase approximation. Later, Turner (2000) developed a complete HWD formulation for a channel domain, by which the author studied the turbulent closure for the inhomogeneous channel flow.

In this paper we combine the HWD theory and our DNS data of turbulent channel flow with streamwise rotation. We perform a scale-polarity decomposition by HWD to analyse the flow in the helical spectral space, such as helical spectrum and nonlinear energy transfer. The helical basis functions will also be used to construct

the IW solutions in the rotating channel. By doing so we try to clarify some puzzling issues on turbulent structures discovered in the streamwise-rotating channel flow, as mentioned by Recktenwald *et al.* (2007, 2009).

The remainder of the paper is organized as follows. In §2, we briefly describe the HWD theory for bounded domains and its applications to viscous incompressible flow. We also derive a new formula for the bounded-domain HWD of the curl of a solenoidal vector field, and a complete set of helical bases for channel domains, which is different from that of Turner (2000). In §3, we apply the general bounded-domain HWD theory to rotating channel flow, with special attention to the form and condition of IW solutions in a channel. In §4, we introduce our DNS results of streamwise-rotating channel turbulence, and apply the numerical HWD to examine the helical-mode statistics and dynamics. In §5, we focus on the IW and long streamwise coherent structures, followed by our conclusion given in §6.

2. General theory and applications to a channel domain

In this section, we make a brief review of the general HWD theory, followed by its specification to a channel domain.

2.1. Helical-wave decomposition for an arbitrary domain

By the well-known HHD, any vector \mathbf{v} defined on a single-connected domain \mathcal{D} can be uniquely decomposed to

$$\mathbf{v} = \mathbf{v}_{\parallel} + \mathbf{v}_{\perp} = \nabla\phi + \nabla \times \boldsymbol{\psi}, \quad (2.1a)$$

with conditions at the domain boundary $\partial\mathcal{D}$

$$\mathbf{n} \cdot \nabla\phi = \mathbf{n} \cdot \mathbf{v}, \quad \mathbf{n} \cdot \mathbf{v}_{\perp} = 0 \quad \text{on } \partial\mathcal{D}, \quad (2.1b)$$

with \mathbf{n} being the unit normal vector pointing out of the domain. Equation (2.1) divides a vector field into a curl-free component \mathbf{v}_{\parallel} and a divergence-free component \mathbf{v}_{\perp} , which will be called the longitudinal and transverse parts, respectively, as in Wu *et al.* (2006).

Then, Yoshida & Giga (1990) proved that the curl operator is self-adjoint if the vector field satisfies the non-penetration boundary. The authors proposed a theorem, which ensures that any transverse vector can be uniquely expanded by a complete set of helical bases $\{\boldsymbol{\phi}_s(\mathbf{x})\}$. Each of the bases is the solution of the eigenproblem

$$\nabla \times \boldsymbol{\phi}_s(\mathbf{x}) = sk\boldsymbol{\phi}_s(\mathbf{x}) \quad \text{on } \mathcal{D}, \quad (2.2a)$$

$$\mathbf{n} \cdot \boldsymbol{\phi}_s(\mathbf{x}) = 0 \quad \text{on } \partial\mathcal{D}, \quad (2.2b)$$

where $s = \pm 1$ is the polarity index and will always be denoted by subscript, and sk is the eigenvalue associated with the eigenfunction $\boldsymbol{\phi}_s(\mathbf{x})$. For the channel domain, due to the capability of separation of variables in the three dimensions of the physical space, the eigenvalue can be written as a wavenumber vector \mathbf{k} , as in a periodic domain. Thus, throughout this paper, we keep using the vector form \mathbf{k} . Clearly, each helical basis corresponds to a Beltramanian field, i.e. the vector field is parallel to its curl everywhere. The helical bases are functionally orthogonal for both different wavenumbers and polarities:

$$\int_{\mathcal{D}} \boldsymbol{\phi}_s(\mathbf{p}, \mathbf{x}) \cdot \boldsymbol{\phi}_t^*(\mathbf{q}, \mathbf{x}) d\mathbf{x} = \delta_{st} \delta_{pq}, \quad (2.3)$$

where the asterisk (*) means complex conjugate and δ is the Kronecker delta. Now, by HHD and HWD one can expand a vector field to

$$\mathbf{v} = \nabla\phi + \sum_s \sum_{\mathbf{k}} \widehat{v}_s(\mathbf{k}) \boldsymbol{\phi}_s(\mathbf{k}, \mathbf{x}), \quad (2.4)$$

where the helical coefficient or amplitude of mode (s, \mathbf{k}) is given by

$$\widehat{v}_s(\mathbf{k}) = \int_{\mathcal{D}} \mathbf{v}(\mathbf{x}) \cdot \boldsymbol{\phi}_s^*(\mathbf{k}, \mathbf{x}) d\mathbf{x}, \quad (2.5)$$

since a potential field $\nabla\phi$ is functionally orthogonal to any helical basis.

One often encounters vector fields as well as their curls in the fluid dynamics, like velocity and its curl, vorticity. While the relation between the helical coefficients of a vector field and its curl is simple for periodic or unbounded domains, it is no longer so in a bounded domain. Rather, we have the following proposition.

PROPOSITION. *If solenoidal vector field \mathbf{v} defined on domain \mathcal{D} has a helical expansion $\mathbf{v} = \sum_{s,\mathbf{k}} \widehat{v}_s(\mathbf{k}) \boldsymbol{\phi}_s(\mathbf{k}, \mathbf{x})$, then its curl $\boldsymbol{\xi} = \nabla \times \mathbf{v}$ will have the helical expansion*

$$\boldsymbol{\xi} = \nabla \times \mathbf{v} = \nabla\varphi + \sum_{s,\mathbf{k}} [sk \widehat{v}_s + b_s(\mathbf{k})] \boldsymbol{\phi}_s, \quad (2.6a)$$

where $\nabla\varphi$ is the longitudinal part of $\boldsymbol{\xi}$, and

$$b_s(\mathbf{k}) = \oint_{\partial\mathcal{D}} \mathbf{n} \cdot [\mathbf{v}(\mathbf{x}) \times \boldsymbol{\phi}_s^*(\mathbf{k}, \mathbf{x})] dS = \oint_{\partial\mathcal{D}} (\mathbf{n} \times \mathbf{v}) \cdot \boldsymbol{\phi}_s^*(\mathbf{k}, \mathbf{x}) dS \quad (2.6b)$$

is the contribution of the boundary.

Proof. Since the curl field $\boldsymbol{\xi}$ may not satisfy the boundary condition (2.2b) although \mathbf{v} does, $\boldsymbol{\xi}$ may have a non-trivial longitudinal part $\nabla\varphi$, with φ being harmonic to make $\mathbf{n} \cdot \boldsymbol{\xi}_{\perp} = 0$. Obviously, if \mathbf{v} consists of finitely many modes, then the curl operator and summation are commutable and $b_s = \varphi = 0$. Generally, when \mathbf{v} consists of infinitely many modes, the operator curl cannot be directly shifted into the summation since the resulting series may not converge. Suppose $\boldsymbol{\xi}$ has expansion

$$\boldsymbol{\xi} = \nabla \times \mathbf{v} = \nabla\varphi + \sum_{s,\mathbf{k}} \widehat{\xi}_s(\mathbf{k}) \boldsymbol{\phi}_s(\mathbf{k}). \quad (2.7)$$

Then by the orthogonal property (2.3), along with Gaussian theorem and (2.2a), one has

$$\begin{aligned} \widehat{\xi}_s(\mathbf{k}) &= \int_{\mathcal{D}} (\nabla \times \mathbf{v} - \nabla\varphi) \cdot \boldsymbol{\phi}_s^* d\mathbf{x} = \int_{\mathcal{D}} \nabla \times \mathbf{v} \cdot \boldsymbol{\phi}_s^* d\mathbf{x} \\ &= \int_{\mathcal{D}} \mathbf{v} \cdot \nabla \times \boldsymbol{\phi}_s^* d\mathbf{x} + \int_{\mathcal{D}} \nabla \cdot (\mathbf{v} \times \boldsymbol{\phi}_s^*) d\mathbf{x} \\ &= sk \int_{\mathcal{D}} \mathbf{v} \cdot \boldsymbol{\phi}_s^* d\mathbf{x} + \oint_{\partial\mathcal{D}} \mathbf{n} \cdot (\mathbf{v} \times \boldsymbol{\phi}_s^*) dS \\ &= sk \widehat{v}_s(\mathbf{k}) + \oint_{\partial\mathcal{D}} (\mathbf{n} \times \mathbf{v}) \cdot \boldsymbol{\phi}_s^* dS, \end{aligned} \quad (2.8)$$

and the proof is completed.

2.2. Helical-wave decomposition of the incompressible Navier–Stokes equation

For an incompressible viscous flow with no-slip and stationary boundary, if velocity \mathbf{u} has helical coefficients $\widehat{u}_s(\mathbf{k})$, then the Proposition indicates that the helical coefficients

of vorticity are

$$\widehat{\omega}_s(\mathbf{k}) = sk \widehat{u}_s(\mathbf{k}), \quad (2.9)$$

where the boundary integral vanishes because $\mathbf{u} \equiv \mathbf{0}$ at the boundary. The coefficients of $\nabla \times \boldsymbol{\omega}$ are

$$\widehat{d}_s(\mathbf{k}) = k^2 \widehat{u}_s + \oint_{\partial \mathcal{D}} (\mathbf{n} \times \boldsymbol{\omega}) \cdot \boldsymbol{\phi}_s^*(\mathbf{k}, \mathbf{x}) dS, \quad (2.10)$$

because usually the tangential component of $\boldsymbol{\omega}$ is not zero at a no-slip boundary.

For such a flow, the continuity equation and Navier–Stokes (NS) equation read, with unit density,

$$\nabla \cdot \mathbf{u} = 0, \quad (2.11a)$$

$$\frac{\partial \mathbf{u}}{\partial t} + \mathbf{l} = -\nabla P + \nu \nabla^2 \mathbf{u}, \quad (2.11b)$$

where $\mathbf{l} = \boldsymbol{\omega} \times \mathbf{u}$ is the Lamb vector, $P = p + |\mathbf{u}|^2/2$ is the total pressure and ν is the kinematic viscosity. As shown by Wu *et al.* (2006), applying HHD to each term of (2.11b), one has the longitudinal and transverse parts as

$$\nabla(P + \psi + \nu \chi) = 0, \quad (2.12a)$$

$$\frac{\partial \mathbf{u}}{\partial t} + \mathbf{l}_\perp = -\nu(\nabla \times \boldsymbol{\omega})_\perp, \quad (2.12b)$$

where ψ and χ are the longitudinal potentials of \mathbf{l} and $\nabla^2 \mathbf{u}$, respectively. Notice that ∇P is purely longitudinal, and \mathbf{u} is a transverse vector because it is divergence-free and vanishes at the boundary.

The longitudinal equation (2.12a) can be integrated once, which gives a Bernoulli-like integral (see Wu *et al.* 2006)

$$P + \psi + \nu \chi = g(t), \quad (2.13)$$

with $g(t)$ being a time-dependent function. On the other hand, by taking curl of (2.12b) one recovers the vorticity equation. Using (2.5), the transverse equation (2.12b) can be fully decomposed by HWD, and the helical amplitude $\widehat{u}_s(\mathbf{k})$ is governed by the dynamical equation

$$\frac{\partial \widehat{u}_s}{\partial t}(\mathbf{k}, t) = -\widehat{l}_s(\mathbf{k}) - \nu \widehat{d}_s(\mathbf{k}), \quad (2.14)$$

where \widehat{l}_s is the helical coefficients of \mathbf{l} . Then, by (2.10), we may cast (2.14) into

$$\left(\frac{\partial}{\partial t} + \nu k^2 \right) \widehat{u}_s = -\widehat{l}_s - \nu \oint_{\partial \mathcal{D}} (\mathbf{n} \times \boldsymbol{\omega}) \cdot \boldsymbol{\phi}_s^*(\mathbf{k}, \mathbf{x}) dS, \quad (2.15)$$

where the second term on the right is a consequence of the Proposition given above.

Equation (2.15) is the general form of the dynamic equation for the helical coefficients in an arbitrary single-connected domain. The boundary integral therein makes wall-bounded flow differ from flow in a periodic box. Previous HWD studies of the homogeneous turbulence belong to the latter case. But on the wall with a no-slip condition, usually the vorticity has a tangential component, thus the boundary integral will affect the time rate of the helical amplitude.

The first term on the right-hand side of (2.15), \widehat{l}_s , represents the influence to the helical amplitude \widehat{u}_s of the nonlinear interactions among helical modes, whose explicit

expression can be derived. By (2.5), we have

$$\widehat{l}_s(\mathbf{k}) = \int_{\mathcal{Q}} \mathbf{l}(\mathbf{x}) \cdot \boldsymbol{\phi}_s^*(\mathbf{k}, \mathbf{x}) \, \mathrm{d}\mathbf{x} = \int_{\mathcal{Q}} (\boldsymbol{\omega} \times \mathbf{u}) \cdot \boldsymbol{\phi}_s^*(\mathbf{k}, \mathbf{x}) \, \mathrm{d}\mathbf{x}. \quad (2.16)$$

As shown before, the velocity and vorticity expansions are

$$\mathbf{u} = \sum_{s_p} \sum_{\mathbf{p}} \widehat{u}_{s_p} \boldsymbol{\phi}_{s_p}(\mathbf{p}, \mathbf{x}), \quad \boldsymbol{\omega} = \sum_{s_q} \sum_{\mathbf{q}} s_q q \widehat{u}_{s_q} \boldsymbol{\phi}_{s_q}(\mathbf{q}, \mathbf{x}), \quad (2.17)$$

where $s_p, s_q = \pm 1$ are the polarity indices associated with the wavenumber vectors \mathbf{p} and \mathbf{q} , respectively. Substituting these into (2.16), and after some algebra, we get

$$\widehat{l}_s(\mathbf{k}) = \sum_{s_p, \mathbf{p}} \sum_{s_q, \mathbf{q}} \widehat{u}_{s_p}(\mathbf{p}) \widehat{u}_{s_q}(\mathbf{q}) I_{s_p s_q}^s(\mathbf{k}|\mathbf{p}, \mathbf{q}) \quad (2.18)$$

with

$$I_{s_p s_q}^s(\mathbf{k}|\mathbf{p}, \mathbf{q}) = \frac{s_p p - s_q q}{2} \int_{\mathcal{Q}} [\boldsymbol{\phi}_{s_p}(\mathbf{p}, \mathbf{x}) \times \boldsymbol{\phi}_{s_q}(\mathbf{q}, \mathbf{x})] \cdot \boldsymbol{\phi}_s^*(\mathbf{k}, \mathbf{x}) \, \mathrm{d}\mathbf{x} \quad (2.19)$$

being the mode-interaction function. It represents the influence on mode (s, \mathbf{k}) of the nonlinear interaction between modes (s_p, \mathbf{p}) and (s_q, \mathbf{q}) . Its simplified version for the periodic box has been derived by Waleffe (1992). However, as discussed in Turner (1999, 2000), for other domains, even as simple as a channel domain, the behaviour of \widehat{l}_s can be much more complex.

The energy equation for each helical mode can be easily derived from (2.14):

$$\frac{1}{2} \frac{\partial}{\partial t} [\widehat{u}_s \widehat{u}_s^*] = N_s(\mathbf{k}) - D_s(\mathbf{k}), \quad (2.20)$$

where

$$N_s(\mathbf{k}) = -\mathrm{Re}[\widehat{l}_s(\mathbf{k}) \widehat{u}_s^*(\mathbf{k})], \quad D_s(\mathbf{k}) = \nu \mathrm{Re}[\widehat{d}_s(\mathbf{k}) \widehat{u}_s^*(\mathbf{k})], \quad (2.21)$$

with ‘ $\mathrm{Re}[\cdot]$ ’ denoting the real part, are the energy transferred into mode (s, \mathbf{k}) by the nonlinear mechanism and the viscous dissipation during the unit time, respectively.

2.3. Helical bases for a channel domain

To conduct an HWD analysis of the flow field in a bounded domain, one has to find the helical bases of that domain. Suppose the channel domain is bounded by two parallel walls at $y = \pm h$, i.e. $(x, y, z) \in [0, L_x] \times [-h, h] \times [0, L_z]$. Hereafter, x , y and z denote the streamwise, normal and spanwise coordinates of the channel, respectively. The details of solving the helical bases are given in Appendix A. Here, for neatness, the bases will be written as

$$\boldsymbol{\phi}_s(\mathbf{k}, \mathbf{x}) = \boldsymbol{\varphi}_s(\mathbf{k}, y) \exp(i\mathbf{k}_\pi \cdot \mathbf{x}_\pi), \quad (2.22)$$

where subscript ‘ π ’ denotes the wall-parallel component of a vector and $\boldsymbol{\varphi}_s(\mathbf{k}, y)$ are the corresponding vector coefficients in (A 4) and (A 5). Notice that bases (A 4) have $\mathbf{k}_\pi = \mathbf{0}$ and are constant in two wall-parallel directions; actually they are the circularly polarized waves given in Kraichnan (1973). Thus, bases (A 4) and (A 5) will be referred to as the average and fluctuating modes, respectively.

Our expression (2.22) differs from that of Turner (2000) in two respects. First, Turner (2000) set two walls at $y = 0$ and $2h$, while we use $y = \pm h$ for the consistency with the computation domain of our DNS. Second, Turner (2000) introduced two

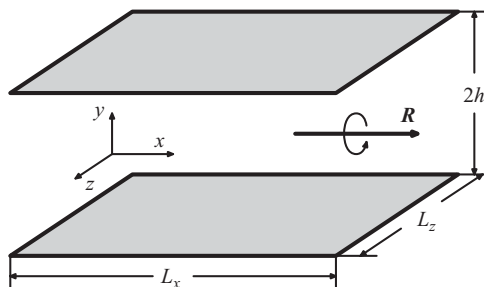


FIGURE 1. The sketch of channel flow with system rotation about an axis \mathbf{R} parallel to the wall.

sets of bases $\Delta(\mathbf{k}, \mathbf{x})$ and $\sigma(\mathbf{k}, \mathbf{x})$ (following the notations there), which satisfy

$$\nabla \times \Delta(\mathbf{k}, \mathbf{x}) = k \sigma(\mathbf{k}, \mathbf{x}), \quad \nabla \times \sigma(\mathbf{k}, \mathbf{x}) = k \Delta(\mathbf{k}, \mathbf{x}). \quad (2.23)$$

Then, these two basis sets were used to decompose a vector field and its curl, respectively. The polarity index s was missing in Turner's two-basis-set formulation. In our study, only one basis set (2.22) is used for all quantities and the polarity index remains, as for the periodic case. By doing so, not only is the computation cost of the numerical HWD smaller (only coding for one set), but also we are allowed to analyse the possible polarity-asymmetry caused by the system rotation.

3. Helical-wave decomposition of rotating channel flow

3.1. Configuration of the rotating channel

As shown in figure 1, we assume that the channel rotates with a constant speed around an axis parallel to the walls. In the rotating frame of reference, the NS equation (2.11b) becomes

$$\frac{\partial \mathbf{u}}{\partial t} + \mathbf{l} + 2\mathbf{R} \times \mathbf{u} = -\nabla P + \nu \nabla^2 \mathbf{u}, \quad (3.1)$$

where \mathbf{R} is the rotating vector of the system and P is the modified total pressure to include the potential of the centrifugal force.

There are two important non-dimensional parameters, the Reynolds number and the rotation number representing the ratio of the Coriolis force to the inertial effect, defined as

$$Re = \frac{Uh}{\nu}, \quad Ro = \frac{2Rh}{U}, \quad (3.2)$$

with $R = |\mathbf{R}|$ and U being a characteristic velocity. The rotation number is the reciprocal of the Rossby number Rs .

3.2. Helical-wave decomposition of the dynamic equation

To apply the theory, one has to find the HWD of the Coriolis force $2\mathbf{R} \times \mathbf{u}$ in (3.1). For \mathbf{R} parallel to the wall, there is

$$\nabla \times (\mathbf{R} \times \phi_s) = -\mathbf{R} \cdot \nabla \phi_s = -i(\mathbf{R} \cdot \mathbf{k}_\pi) \phi_s = -\frac{i s (\mathbf{R} \cdot \mathbf{k}_\pi)}{k} \nabla \times \phi_s, \quad (3.3)$$

where (2.2a) has been used for deriving the last equality. We thus find

$$\mathbf{R} \times \phi_s = -\frac{i s (\mathbf{R} \cdot \mathbf{k}_\pi)}{k} \phi_s + \nabla \psi_s, \quad (3.4)$$

in which a harmonic potential ψ_s is introduced to satisfy the boundary condition. Then, the helical coefficient of the Coriolis force is

$$\hat{c}_s(\mathbf{k}) = \int_{\mathcal{D}} \left(2\mathbf{R} \times \sum_{s,p} \hat{u}_s \boldsymbol{\phi}_s(\mathbf{p}, \mathbf{x}) \right) \cdot \boldsymbol{\phi}_s^*(\mathbf{k}, \mathbf{x}) d\mathbf{x} = -\frac{i2s(\mathbf{R} \cdot \mathbf{k}_\pi)}{k} \hat{u}_s. \quad (3.5)$$

Notice that when $\mathbf{R} \cdot \mathbf{k}_\pi = 0$, we have $\hat{c}_s(\mathbf{k}) = 0$, indicating that the Coriolis force does not affect the helical modes whose \mathbf{k}_π is perpendicular to the rotating axis.

In the rotating frame of reference, the dynamic equation (2.14) for $\hat{u}_s(k)$ is now generalized to

$$\frac{\partial \hat{u}_s}{\partial t} = -\hat{l}_s(\mathbf{k}) - \nu \hat{d}_s(\mathbf{k}) + \frac{i2s(\mathbf{R} \cdot \mathbf{k}_\pi)}{k} \hat{u}_s. \quad (3.6)$$

Similarly, to the kinetic energy equation (2.20) we need to add the Coriolis term

$$\text{Re}[\hat{c}_s(\mathbf{k}) \hat{u}_s^*(\mathbf{k})] = \text{Re} \left[-\frac{i2s(\mathbf{R} \cdot \mathbf{k}_\pi)}{k} \hat{u}_s \hat{u}_s^* \right] = 0, \quad (3.7)$$

i.e. the Coriolis force only affects the phase angle of the helical coefficient $\hat{u}_s(\mathbf{k})$ when \mathbf{k} is not perpendicular to the rotating axis, and does not change the amount of kinetic energy carried by each helical mode. Thus, the energy equation for a rotating channel is precisely the same as (2.20). For a rotating channel with \mathbf{R} parallel to the walls, the time rate of the kinetic energy is still determined by $N_s(\mathbf{k})$, which is the nonlinear energy transferred into mode (s, \mathbf{k}) via the nonlinear interaction, and $D_s(\mathbf{k})$, the viscous dissipation.

3.3. The inertial waves in channel flow

As addressed by Greenspan (1969), an unbounded rotating fluid may carry inviscid IW. This kind of wave may still exist in a bounded fluid with system rotation. Maas (2003) solved the IW for the channel rotating around the axis perpendicular to the walls. Now, by the helical basis functions (2.22), we can construct the IW solutions for the channel domain rotating around the axis parallel to the wall. The methodology is similar to that in Greenspan (1969) and Waleffe (1993). In doing so, we assume the waves are effectively inviscid.

For fluid in a channel domain without basic flow, the IW solution and its characteristics are very similar to those in an infinite domain, which are reported in Appendix B. Here, we only consider the IW in a channel with basic mean flow, and will compare the theory with the numerical results in §5.

Suppose the channel has a steady mean flow with velocity and vorticity profiles denoted by $\mathbf{U}(y)$ and $\boldsymbol{\Omega}(y)$, and the fluctuating part denoted by \mathbf{u} and $\boldsymbol{\omega}$, respectively. We now look for possible IW solutions and the conditions for their existence. The inviscid equation of the fluctuating vorticity reads

$$\frac{\partial \boldsymbol{\omega}}{\partial t} + \nabla \times \mathbf{l} + \mathbf{u} \cdot \nabla \boldsymbol{\Omega} - \boldsymbol{\omega} \cdot \nabla \mathbf{U} = 2\mathbf{R} \cdot \nabla \mathbf{u} + \boldsymbol{\Omega} \cdot \nabla \mathbf{u} - \mathbf{U} \cdot \nabla \boldsymbol{\omega}, \quad (3.8)$$

where $\mathbf{l} = \boldsymbol{\omega} \times \mathbf{u} - \overline{\boldsymbol{\omega} \times \mathbf{u}}$. Hereafter, the overline means taking the average over (x, z) plane and time.

By the form of the basis (2.22), assume the equation has the formal solution

$$\left. \begin{aligned} \mathbf{u} &= \boldsymbol{\varphi}_s(\mathbf{k}, y) \exp[i(\mathbf{k}_\pi \cdot \mathbf{x}_\pi - f_s t)], \\ \boldsymbol{\omega} &= s\mathbf{k} \boldsymbol{\varphi}_s(\mathbf{k}, y) \exp[i(\mathbf{k}_\pi \cdot \mathbf{x}_\pi - f_s t)], \end{aligned} \right\} \quad (3.9)$$

which leads to $\mathbf{l} \equiv \mathbf{0}$. The frequency f_s will be determined later. The last two terms on the left-hand side of (3.8) can be cast as

$$\mathbf{u} \cdot \nabla \boldsymbol{\Omega} - \boldsymbol{\omega} \cdot \nabla \mathbf{U} = u_y (\partial_y \boldsymbol{\Omega} - sk \partial_y \mathbf{U}), \quad (3.10)$$

where ∂_y stands for the partial derivative with respect to y . Then, if the above expression vanishes or the mean flow satisfies an IW condition,

$$\partial_y \boldsymbol{\Omega} = sk \partial_y \mathbf{U} \quad \text{or} \quad \boldsymbol{\Omega} - sk \mathbf{U} = 2\mathbf{C}_\pi, \quad (3.11)$$

with \mathbf{C}_π being a wall-parallel constant vector, one obtains a dispersion relation

$$f_s = -2s(\mathbf{R} + \mathbf{C}_\pi) \cdot \boldsymbol{\kappa} = -2s\mathbf{R}_{ef} \cdot \boldsymbol{\kappa}, \quad (3.12)$$

where the effective angular speed $\mathbf{R}_{ef} = \mathbf{R} + \mathbf{C}_\pi$ and $\boldsymbol{\kappa} = \mathbf{k}/k$. This formula has the same form as (B 2). Thus, a mean flow satisfying the IW condition (3.11) allows for the IW solution (3.9) and modifies the angular velocity \mathbf{R} by a constant vector \mathbf{C}_π . The phase and group velocities are also modified to

$$\mathbf{c}_p = -\frac{2s\mathbf{R}_{ef} \cdot \boldsymbol{\kappa}}{|\mathbf{k}_\pi|^2} \mathbf{k}_\pi, \quad (3.13)$$

$$\mathbf{c}_g = -\frac{2s}{k^3} [k_y^2 \mathbf{R}_{ef} + \mathbf{k}_\pi \times (\mathbf{R}_{ef} \times \mathbf{k}_\pi)], \quad (3.14)$$

respectively.

The IW condition (3.11) requires that the two vectors $\partial_y \boldsymbol{\Omega}$ and $\partial_y \mathbf{U}$ must be parallel to each other, and fixes the magnitude of the wavenumber vector as

$$K_{in} = |\partial_y \boldsymbol{\Omega}|/|\partial_y \mathbf{U}|. \quad (3.15)$$

Moreover, the polarity of the inertial wave is +1 or −1 if $\partial_y \boldsymbol{\Omega}$ and $\partial_y \mathbf{U}$ are in the same or opposite direction, respectively. We will verify the theoretical predictions by the numerical results in §5.

4. Numerical simulations and turbulence statistics

In this section, we present our numerical HWD analysis. We have carried out DNS for \mathbf{R} pointing to both streamwise and spanwise directions; however, in this paper, we focus solely on the former case. We first describe the DNS method and the characteristics of the mean flow in a streamwise-rotating channel. We then apply HWD to the data to display the statistical dynamics of the helical modes.

4.1. Numerical method and mean-flow statistics

Our DNS employs the classic pseudospectral method as in Kim, Moin & Moser (1987). For spatial discretization, it uses the Fourier–Chebyshev expansion, while for temporal evolution, convection and viscous terms are advanced by the explicit Adams–Bashforth and implicit Crank–Nicolson schemes, respectively. The Coriolis force is treated as the convection term. The 3/2 rule is utilized for the de-aliasing of the nonlinear term. Several different rotation rates were computed. The initial condition for the rotating cases was taken as an instantaneous field extracted from a non-rotating fully developed turbulent channel flow. All the flows are driven by a constant mean pressure gradient in the streamwise direction. The length and velocity are non-dimensionalized by the channel half-height h and the wall-friction velocity $u_{\tau 0}$ of the initial non-rotating channel flow, which has a Reynolds number $Re_{\tau 0} = u_{\tau 0} h / \nu = 180$.

Case	Ro	$L_x \times 2h \times L_z$	$N_x \times N_y \times N_z$	Rs_b	Re_b	K_{in}
ST5	5	$4\pi \times 2 \times 2\pi$	$128 \times 129 \times 128$	3.104	2793.5	5.070
ST10	10	$4\pi \times 2 \times 2\pi$	$128 \times 129 \times 128$	1.497	2694.1	5.345
ST10F	10	$4\pi \times 2 \times 4\pi$	$128 \times 129 \times 128$	1.438	2587.6	4.953
ST20	20	$4\pi \times 2 \times 2\pi$	$128 \times 129 \times 128$	0.676	2435.0	4.770
ST20F	20	$4\pi \times 2 \times 4\pi$	$128 \times 129 \times 128$	0.644	2319.6	4.645
ST30	30	$8\pi \times 2 \times 4\pi$	$256 \times 129 \times 256$	0.413	2230.1	5.255

TABLE 1. The parameters used in DNS, and statistics of the flows.

The corresponding rotation number is defined as $Ro = 2Rh/u_{\tau 0}$. In addition, based on the mean bulk velocity in the streamwise direction, the global Reynolds number and Rossby number are given by

$$Re_b = \frac{hU_b}{\nu}, \quad Rs_b = \frac{U_b}{2Rh} \quad \text{with} \quad U_b = \frac{1}{2h} \int_{-h}^h U(y) dy. \quad (4.1)$$

These parameters of the DNS are listed in table 1.

It is well known that when a streamwise rotation is applied to the channel and pipe flow, very long structures appear in the central flow region, e.g. the experiments and DNS of the channel flow by Recktenwald *et al.* (2007) and the DNS of the pipe flow by Orlandi & Fatica (1997). Thus, the streamwise length of the computational domain must be long enough to capture these structures. Wu & Kasagi (2004) used a $5\pi \times 2 \times 2\pi$ box for the streamwise rotating rate up to $Ro = 15$. Oberlack *et al.* (2006) and Recktenwald *et al.* (2007) chose $4\pi \times 2 \times 2\pi$ for $Ro \leq 6.5$ and doubled the sizes in (x, z) directions for larger Ro . In our simulations, the box sizes at lower Ro are the same (for $Ro = 5$) or smaller (for $Ro = 10, 20$) than the aforementioned ones; however, at the largest $Ro = 30$, we double the lengths in both the x and z directions. It should be mentioned that the streamwise lengths in this study are comparable to that of the pipe in Orlandi & Fatica (1997) for similar rotation numbers. The sufficiency of the box sizes will be further discussed later by the two-point correlation.

The total computation time is $80h/u_{\tau 0}$ for ST05 and $100h/u_{\tau 0}$ for other cases. The statistics are sampled over the last $40h/u_{\tau 0}$ after the flow reaches a steady state, i.e. the total energy fluctuating around a constant value and the total shear stress reaching a linear profile. Although the time duration for sampling is much shorter than that of Recktenwald *et al.* (2007) ($\approx 172h/u_{\tau 0}$) and Oberlack *et al.* (2006) ($225u_{\tau 0}/h$), it is longer than that of Wu & Kasagi (2004) ($12h/u_{\tau 0}$) and comparable with that of Alkishriwi *et al.* (2008) ($\approx 42h/u_{\tau 0}$). We believe the value is sufficient for computing the statistics. In figure 2 the mean-velocity profiles U and W are plotted. The streamwise mean velocity decreases as Ro increases, and an antisymmetric secondary mean flow develops in the spanwise direction. In this study, the system rotation is in the anticlockwise direction; thus, in figure 2(b), the two peaks near the walls (referred to as the outboard peaks) are in the same direction as the system rotation, while the two peaks near the centreline (referred to as the inboard peaks) are in the opposite direction to the system rotation. This tendency has been found by many simulations such as Wu & Kasagi (2004), Oberlack *et al.* (2006), Recktenwald *et al.* (2007) and Recktenwald *et al.* (2009). When Ro becomes larger, the outboard peaks of W are stronger, while the reverse flow at the centre region first increases for Ro from 5 to 20, then decreases for $Ro = 30$. It seems that to fully clarify this non-monotonic trend,

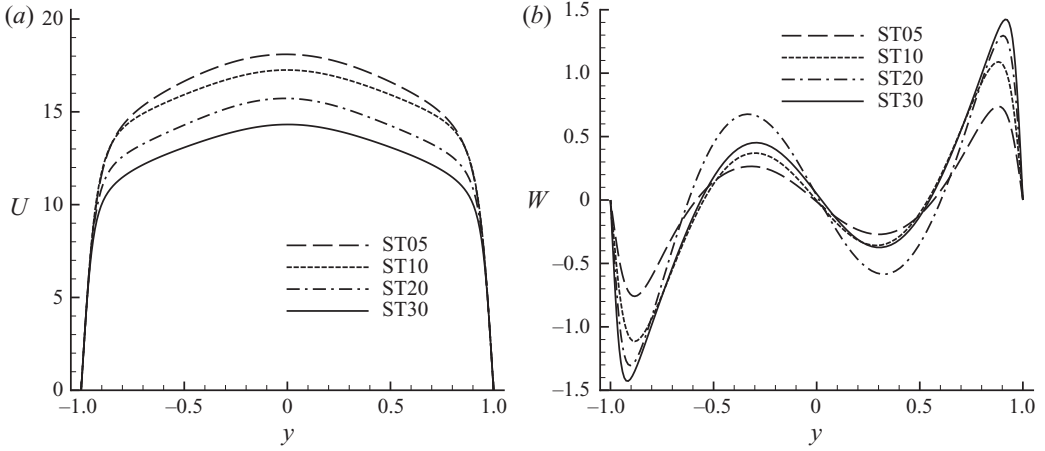


FIGURE 2. The profiles of the mean flows in the streamwise and spanwise directions.

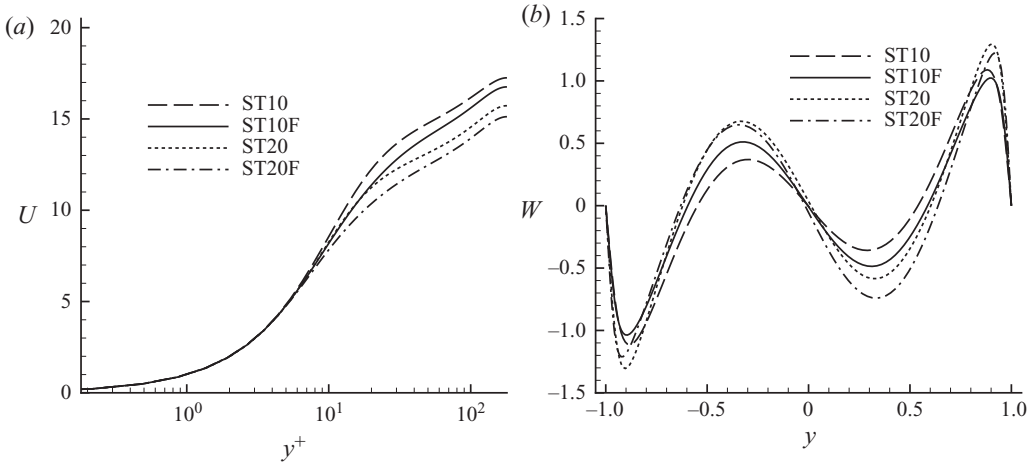


FIGURE 3. Comparisons of the mean profiles between two different domain sizes for $Ro = 10$ and 20. (a) Only half of the channel is shown in wall unit.

one needs simulation at even larger Ro . Later, we will show that other statistics also have non-monotonic dependence on Ro .

In order to observe the effect of the domain size, we double the spanwise length of L_z for $Ro = 10$ and 20 but keep the streamwise length L_x the same, as listed in table 1. Figure 3 plots the mean-velocity profiles for Cases ST10, ST10F, ST20 and ST20F. The increase of L_z reduces the streamwise mean velocity at the central region, but hardly changes its near-wall behaviour. Meanwhile, the outboard W peaks decrease and the inverse flow at the channel centre is enhanced when L_z is doubled. These phenomena may imply that the mean velocity for the streamwise-rotating channel is affected by the domain size, or the aspect ratio L_x/L_z . Alkishriwi *et al.* (2008) stated that L_z in the order of $10h$ should be sufficient to use periodic conditions in the spanwise direction. To clarify the domain-size influence, more simulations with different channel configurations are necessary, which we leave as an open issue. Our focus below is the underlying physics in the streamwise-rotating channel, such as the mechanism of the reverse spanwise flow and the flow structures.

4.2. Numerical helical-wave decomposition investigation and energy spectra

To conduct the HWD analysis of the flow data obtained by DNS, the flow fields stored during the simulations were projected onto the HWD bases (2.22) afterwards. Since in the x and z directions both DNS and HWD employ the Fourier expansion, the fast Fourier transform (FFT) is applicable for these homogeneous directions. In the wall-normal direction, one needs to transform from the Chebyshev polynomial $T_j(y)$ ($j = 0, \dots, N$, with N being the highest order of the polynomials) in DNS to the vector coefficients $\boldsymbol{\varphi}_s(\mathbf{k}, y)$ in HWD bases (2.22). Actually, the transformation matrix between these two bases is given by

$$\mathbf{M}_{sj}(\mathbf{k}) = \int_{-h}^h T_j(y) \boldsymbol{\varphi}_s^*(\mathbf{k}, y) dy, \quad (4.2)$$

and can be computed explicitly prior to the numerical HWD. Then the helical coefficient is given by

$$\widehat{u}_s(\mathbf{k}) = \sum_{j=0}^N \widetilde{u}_j \cdot \mathbf{M}_{sj}(\mathbf{k}), \quad (4.3)$$

where \widetilde{u}_j is the coefficient of the Fourier–Chebyshev expansion in DNS. More details are reported in Yang (2009).

In the following HWD investigation, we focus on four cases, which are ST05, ST10F, ST20F and ST30. Based on the helical coefficients of the velocity field, the helical energy spectrum is defined for the fluctuating flow as

$$E_s(k) = \frac{1}{2} \sum_{I(k)}^{|k_x| \neq 0} \widehat{u}_s(\mathbf{k}) \widehat{u}_s^*(\mathbf{k}), \quad (4.4)$$

with $I(k)$ being an interval of the magnitude of the wavenumber vectors with mid-point k . Throughout this paper, the interval width is set to be $\pi/2$ since the wall-normal wavenumber k_y has the largest step size of $\pi/2$ among the three components of \mathbf{k} . The fluctuating energy contained in a single polarity is $E_{as} = \sum_k E_s(k)$.

For a non-rotating channel, our numerical results have revealed that the energy is evenly distributed between two polarities (not shown here). For a rotating channel, the time history of the ratios E_{a-}/E_{a+} , an indicator for the polarity-symmetry, is plotted in figure 4. Clearly, the streamwise rotation induces an asymmetry between opposite polarities. The fact $E_{a-}/E_{a+} > 1$ for all cases indicates that the negative polarity with $s = -1$ contains more energy than the positive one. This asymmetry becomes stronger as Ro increases up to 20. But it seems that the ratio is smaller for $Ro = 30$ than that of $Ro = 20$.

The non-monotonic dependence of E_{a-}/E_{a+} on Ro is of interest because similar non-monotonicity has also been discovered in a spanwise-rotating channel (Grundestam *et al.* 2008) and decaying turbulence (Bourouiba & Bartello 2007). To see if the domain size is a factor, we compare in figure 5 the same ratio for different box sizes with $Ro = 10$ and 20. The curves indicate that extending the computing box from $4\pi \times 2\pi$ to $4\pi \times 4\pi$ only slightly affects the polarity-asymmetry. Thus, very likely, the non-monotonic dependence of E_{a-}/E_{a+} on Ro is not solely caused by the domain size. However, as pointed out by one of the referees, to achieve a conclusive clarification it would be highly desirable to perform more simulations with the same domain for different rotation rates.

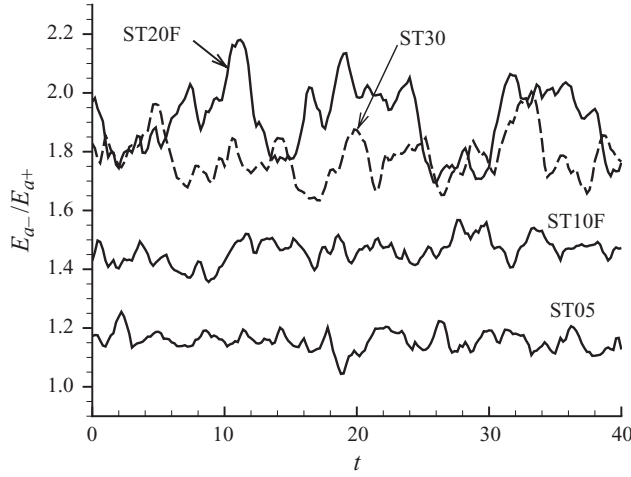


FIGURE 4. The time history of the ratios E_{a-}/E_{a+} , i.e. the ratios of the energy contained in two opposite polarities.

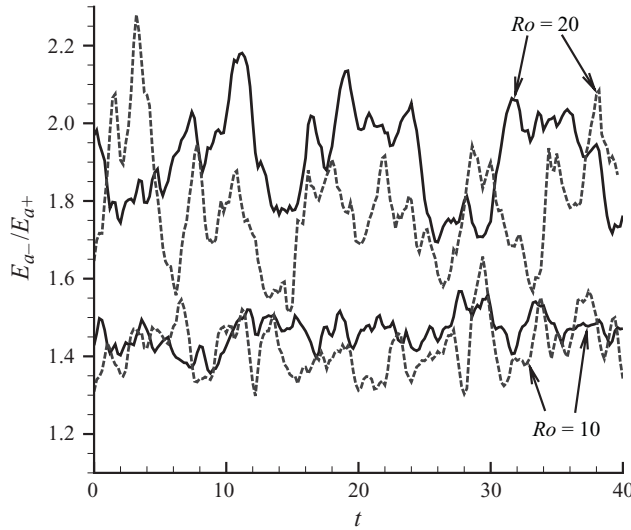


FIGURE 5. Box-size effect on the ratios E_{a-}/E_{a+} . Black solid lines, $4\pi \times 4\pi$; grey dashed lines, $4\pi \times 2\pi$.

In figure 6 the normalized time-averaged spectra $E_s(k)$ are plotted for all four different rotation numbers Ro . In this subsection, all the spectra are normalized by the respective total fluctuating energy of each case. A remarkable feature is that as Ro increases, the energy tends to concentrate to the modes with negative polarity and certain wavenumber. For Case ST05, a dominant wavenumber does not yet form. But for higher rotating rates, the wavenumbers with the highest energy fall into the same interval $I(K_m)$, with $K_m = 3\pi/2$ denoting the dominant wavenumber. Compared to the non-rotating case, the streamwise rotation induces the large scales (small k) containing more energy, especially for the negative polarity. The energy carried by small scales (large k) are slightly less than that of the non-rotating case. The coherent structures responsible for this feature will be addressed in § 5.

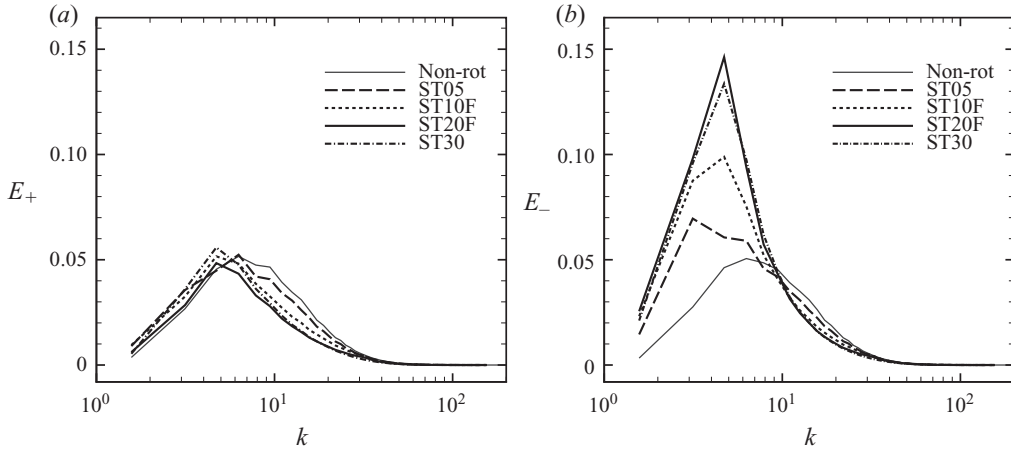


FIGURE 6. The time-averaged helical spectra for each polarity. (a) $s = 1$; (b) $s = -1$.

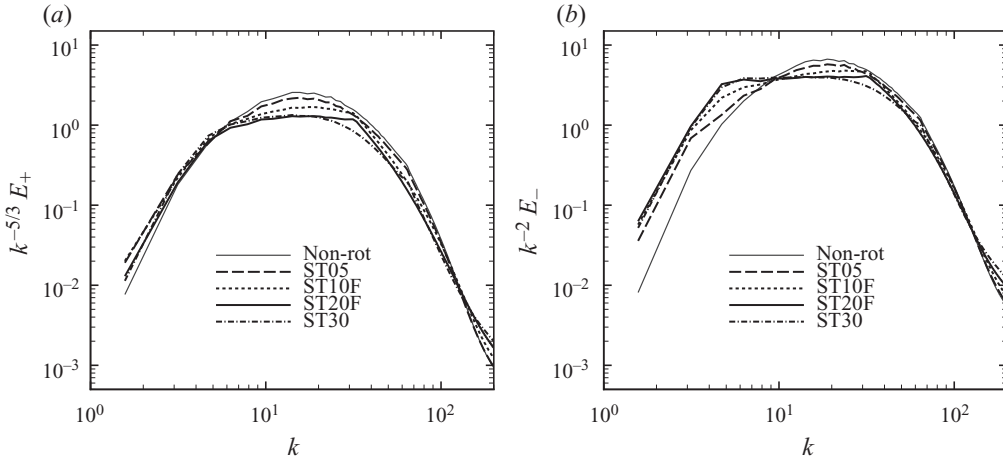


FIGURE 7. The time-averaged compensated spectra for each polarity. (a) $s = 1$, $k^{-5/3} E_+$; (b) $s = -1$, $k^{-2} E_-$.

In homogeneous turbulence with background rotation, it is well known that the strong system rotation causes the scaling law of the energy spectra to depart from $k^{-5/3}$. When forced at a certain wavenumber k_f , a k^{-2} scaling appears at the region $k > k_f$ despite the different choices of k_f (e.g. see Yeung & Zhou 1998; Smith & Waleffe 1999; Mininni, Alexakis & Pouquet 2009; Thiele & Müller 2009). For the streamwise-rotating channel, it is reasonable to regard the most energetic wavenumber K_m as the forced one. (In the next subsection, we will further show that K_m is also the wavenumber obtaining energy from the mean flow at the highest rate.) In figure 7 the compensated energy spectra are plotted for each polarity in a full log scale. Interestingly, as Ro becomes larger, the spectrum $E_+(k)$ develops a distinct $k^{-5/3}$ scaling region similar to the non-rotating homogeneous turbulence, while a k^{-2} scaling appears in the spectrum $E_-(k)$ at region $k > K_m = 3\pi/2$, which is similar to the rotating homogeneous case. These two regions with different scaling laws are quite

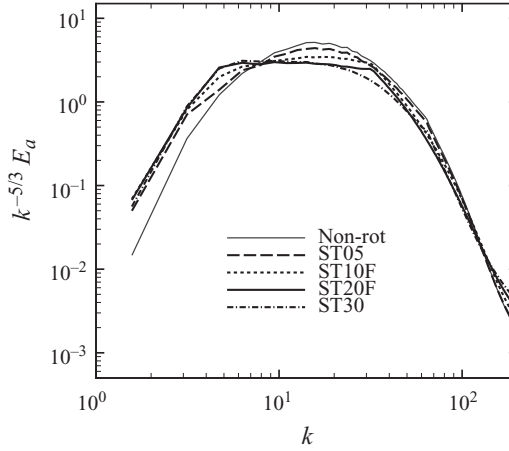


FIGURE 8. The time-averaged compensated total spectra $k^{-5/3} E_a(k)$.

obvious for rotating rates $Ro = 20$ and 30 . The plots also show that the scaling region of Case ST20F is broader than Case ST30.

Figure 8 shows the compensated spectra of the total fluctuating energy. Although the negative polarity contains more energy than the positive one, the total energy spectra shows a $k^{-5/3}$ scaling as the E_+ spectra. Smith & Waleffe (1999) found that the total spectra obeyed a $k^{-5/3}$ scaling when $Rs = 0.35$ and changed to k^{-2} for $Rs = 0.17$, where the Rossby number was defined as $Rs = (k_f^2 \epsilon_f)^{1/3} / R$ based on the external energy input rate ϵ_f and the forcing wavenumber k_f . For channel flow, a similar Rossby number may be defined as $Rs_p = (K_m^2 U_b \partial_x P)^{1/3} / R$, where $\partial_x P$ is the mean pressure gradient and $U_b \partial_x P$ may be regarded as a energy input rate. For Case ST30 there is $Rs_p \approx 0.43$. Hence, the rotation in our simulations may not be strong enough to alter the total spectra. It is of significant interest to further explore in the future whether these different scaling laws are a general trend and what is the underlying mechanism.

4.3. Nonlinear energy transfer

We now investigate the energy transfer caused by the nonlinear interactions among the helical modes. As indicated by the kinetic energy equation (2.20), the time rate of the kinetic energy in each helical mode is determined by two effects, the nonlinear interaction and the viscous dissipation. The pressure term is projected out when conducting HWD to the NS equation. The energy transfer function may be defined as

$$T_s(k) = \sum_{I(k)}^{|k_\pi| \neq 0} N_s(\mathbf{k}), \quad (4.5)$$

which denotes the amount of the energy flowing into the modes with $|\mathbf{k}| \in I(k)$ and polarity s during the unit time. The total dissipation for the fluctuating flow is $D_a = \nu \sum_{s,k} D_s(\mathbf{k})$. In this subsection, all the transfer functions are normalized by D_a for each case.

Since the energy spectra have shown asymmetry between two polarities, one also expects the asymmetry between T_+ and T_- . Figure 9 shows that this is indeed so. The maximal values of T_+ are reduced for three cases with $Ro \geq 10$, while a new strong peak appears at K_m in T_- curves for $Ro = 20$ and 30 . Therefore, the most favourable

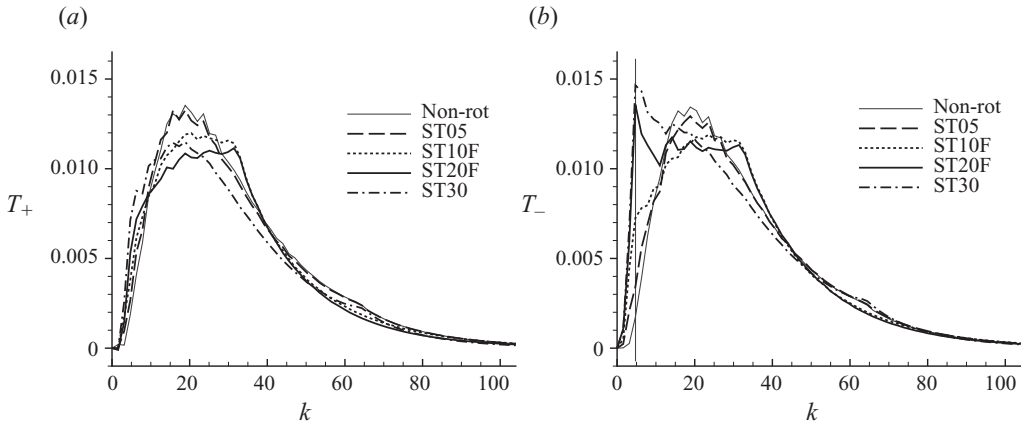


FIGURE 9. The total energy transfer functions T_s . In (b) and the following figures the vertical line always marks the most energetic wavenumber K_m . (a) $s = 1$; (b) $s = -1$.

modes, i.e. with wavenumber K_m and negative polarity, gain energy at the highest rate. Both T_+ and T_- are positive for almost all wavenumbers. Thus, the fluctuating modes obtain energy at all scales, which can only be from the mean flow.

In order to investigate the nonlinear energy transfer in more detail, we decompose the transfer function into three distinct parts. In the physical space, the fluctuating part of the NS equation can be written as

$$\frac{\partial \mathbf{u}}{\partial t} + \mathbf{L} + 2\mathbf{R} \times \mathbf{u} = -\nabla P' + \nu \nabla^2 \mathbf{u}, \quad (4.6)$$

where P' is the fluctuating part of the modified pressure P and the fluctuating Lamb vector \mathbf{L} can be divided into

$$\mathbf{L} = \mathbf{l}_1 + \mathbf{l}_2 + \mathbf{l}_3 = \boldsymbol{\Omega} \times \mathbf{u} + \boldsymbol{\omega} \times \mathbf{U} + (\boldsymbol{\omega} \times \mathbf{u} - \overline{\boldsymbol{\omega} \times \mathbf{u}}). \quad (4.7)$$

Throughout this subsection, $(\mathbf{U}, \boldsymbol{\Omega})$ denote the mean flow and $(\mathbf{u}, \boldsymbol{\omega})$ denote the fluctuating quantities. Applying HWD to \mathbf{L} , three different nonlinear functions and the transfer functions can be defined, as in (2.20),

$$N_{is}(\mathbf{k}) = -\text{Re}[\widehat{l}_{is}(\mathbf{k})\widehat{u}_s^*(\mathbf{k})], \quad T_{is}(k) = \sum_{|k_\pi| \neq 0} N_{is}(\mathbf{k}), \quad (4.8)$$

where \widehat{l}_{is} , with $i = 1, 2, 3$, are the helical coefficients of \mathbf{l}_i in (4.7). By their corresponding terms in the physical space as given by (4.7), one may interpret T_1 and T_2 as the nonlinear interactions between the fluctuating modes and the mean flow, and T_3 as the nonlinear interactions among the different fluctuating modes.

By the definitions of \mathbf{l}_i , it is apparent that $\mathbf{u} \cdot \mathbf{l}_1 \equiv 0$ and $\int \mathbf{u} \cdot \mathbf{l}_3 \, d\mathbf{x} = 0$, thus the corresponding transfer functions satisfy

$$\sum_{k,s} T_{1s}(k) = \sum_{k,s} T_{3s}(k) = 0. \quad (4.9)$$

In other words, T_1 and T_3 do not change the total fluctuating energy, but only affect the energy distribution among the wavenumbers and polarities. Thus, according to the general form of the energy equation (2.20), the equation for the total fluctuating

energy $E_a(t) = E_{a+} + E_{a-}$ reads

$$\frac{\partial E_a(t)}{\partial t} = \sum_{k,s} T_{2s}(k, t) - D_a(t). \quad (4.10)$$

Then, when the turbulent channel flow has reached the steady state, after a long-time average one has

$$D_a = \sum_{k,s} T_{2s}, \quad (4.11)$$

namely the total dissipation is solely balanced by the T_2 term from a long-time view.

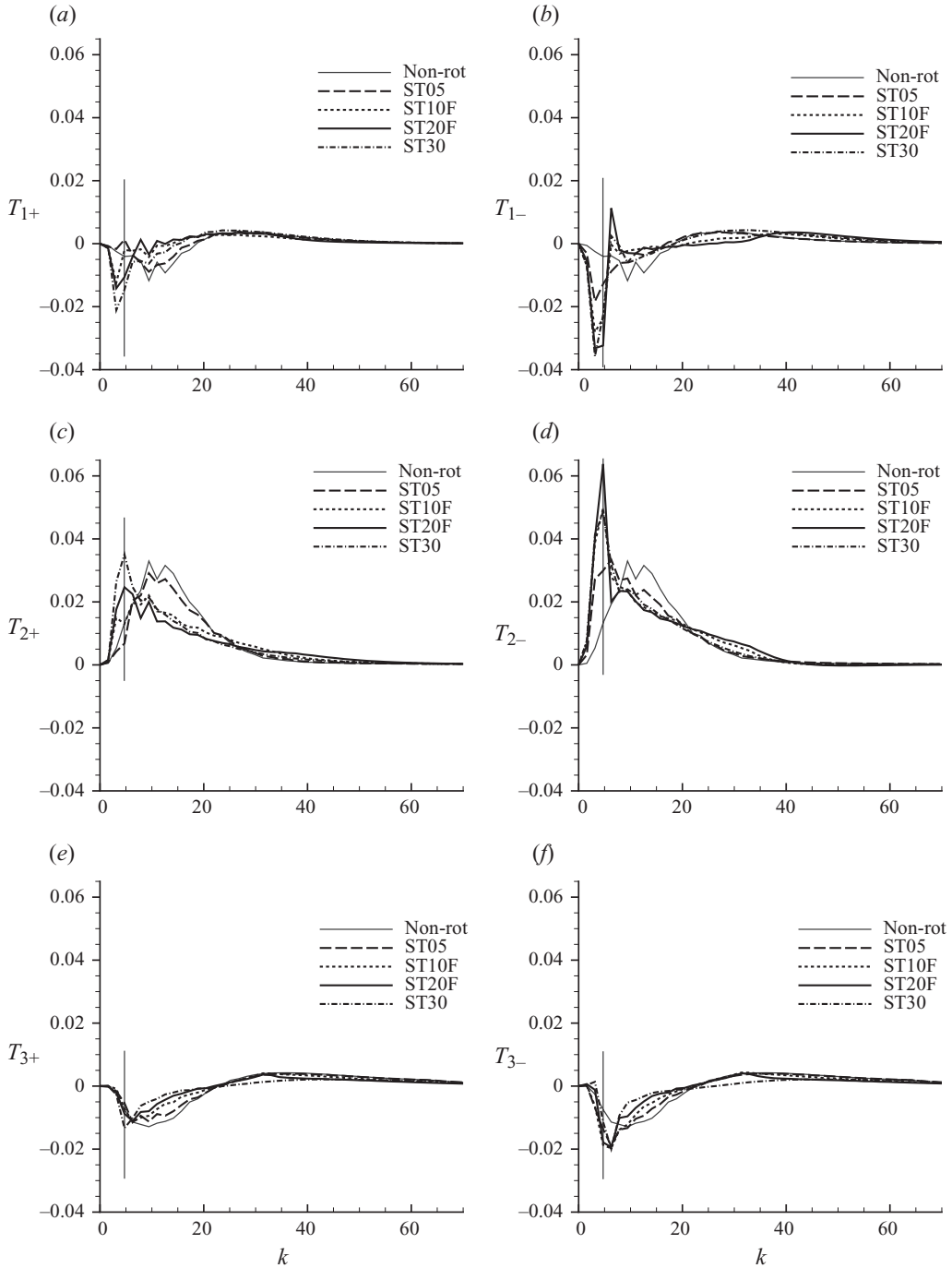
In figure 10 the three transfer functions are shown for four rotating rates. The T_1 and T_2 curves reveal two different effects of the mean flow on the fluctuating modes. First, T_{2s} is positive for all wavenumbers, thus this term induces the energy flowing into the fluctuating modes. This energy may only come from the mean flow. The streamwise rotation shifts the T_2 maxima to the wavenumber K_m of the most energetic helical modes, as shown in figure 6. For Case ST05, the T_{2-} peak has moved towards K_m , while the T_{2+} curve only changes slightly compared with the non-rotating case. For the three cases with bigger Ro , both T_{2s} with $s = \pm 1$ reach the maxima at K_m , but the negative polarity has stronger peak than the positive one.

We have explained that the T_1 term does not change the total fluctuating energy but represents a redistribution of the turbulent energy among the helical modes under the influence of the mean flow. As the second effect of the mean flow on the fluctuating modes, the T_1 curves in figure 10(a) further indicate that the large scales lose energy and the small scales gain energy. The negative peaks are not located at K_m , but at a wavenumber slightly smaller than K_m . On the other hand, the T_3 term represents the energy transfer caused by the nonlinear interaction between the fluctuating modes. The overall behaviour of T_{3s} is similar to that of T_{1s} , i.e. negative at large scales and positive at small scales. Notice that the location of T_{3-} minima stay at the wavenumber slightly larger than K_m . It is interesting that for $s = -1$ the locations of T_{i-} extrema for different i do not coincide with each other. Specifically, the most energetic modes with $k \in I(K_m)$, which obtain energy at the highest rate via T_{2-} , lose energy at a smaller rate via T_{1-} and T_{3-} than those at the adjacent wavenumbers. Thus, the net rate of the energy transfer into the interval $I(K_m)$ has the largest value, as shown in figure 9(b).

5. Inertial waves and long inclined vortex clusters

5.1. Inertial waves

We have shown in §4.1 that the secondary mean flow W in the spanwise direction has a reverse profile at the central region of the channel. This phenomenon has also been discovered, to our knowledge, in all the numerical simulations of the streamwise-rotating channel flow in the existing literature. Oberlack *et al.* (2006) stated that this reverse W profile was unlikely to be caused by the large-scale structure because no such structure was found in the flow visualization. Later Recktenwald *et al.* (2007) conducted a similar DNS, where a reverse region appeared again in the W profile. Based on the extended correlation area in the streamwise direction as the rotation speed increases, the authors attributed the phenomenon to the turbulent structures with very long streamwise scales. However, a major discrepancy showed up when Recktenwald *et al.* (2007) compared their numerical and experimental results. In the latter, the reverse W region can hardly be detected. To minimize the difference between

FIGURE 10. The energy transfer functions T_{is} for four different Ro .

the boundary conditions of the DNS and experiments, Recktenwald *et al.* (2009) replaced the periodic condition by two endwalls in the spanwise direction in their LES. Although the reverse flow was reduced, it still exists in the LES results. Nevertheless,

the two-point correlations in the streamwise direction of the experimental fields are always smaller than that of the numerical data. Thus, in the numerical simulation, there must be some structures with large streamwise scale.

This puzzling issue can be well clarified by the existence of IW associated with vortical structures specifically for the turbulence in a streamwise-rotating channel. On the one hand, in the preceding section we saw that in the streamwise-rotating channel, the energy concentrates to certain helical modes with particular wavenumber and polarity. On the other hand, we have shown in §3.3 that by the helical basis functions one can construct the IW solutions, as long as the mean flow satisfies the IW condition (3.11). In the channel flow with the spanwise rotation, as shown by many experimental and numerical results such as Johnston *et al.* (1972), Kristoffersen & Andersson (1993) and Grundestam *et al.* (2008), the mean velocity $\mathbf{U}(y)$ only has the streamwise component and thus the mean vorticity $\boldsymbol{\Omega}(y)$ is along the spanwise direction. Hence, $\partial_y \boldsymbol{\Omega}$ and $\partial_y \mathbf{U}$ cannot be parallel to each other and no IW solution exists. However, in the streamwise-rotating channel, a mean secondary flow develops in the spanwise direction, which indicates that \mathbf{U} and $\boldsymbol{\Omega}$ have both the streamwise and spanwise components. In this case, the inertial-wave solutions may exist.

Further information about the mean basic flow can be deduced from the IW condition (3.11) for the streamwise-rotating channel. Let $U(y)$ and $W(y)$ be the mean streamwise and spanwise velocity, respectively, such that $\boldsymbol{\Omega}(y) = (\partial_y W, -\partial_y U)$. The substitution of this into (3.11) gives

$$\frac{\partial \Omega_x}{\partial y} = \frac{\partial^2 W}{\partial y^2} = sk \frac{\partial U}{\partial y}, \quad \frac{\partial \Omega_z}{\partial y} = -\frac{\partial^2 U}{\partial y^2} = sk \frac{\partial W}{\partial y}. \quad (5.1)$$

Oberlack *et al.* (2006) and our DNS have showed that $\partial_y U = 0$ and $W = 0$ at $y = 0$. Then the above equations have the solution

$$U = A \cos(K_{in} y) + U_0, \quad (5.2a)$$

$$W = sA \sin(K_{in} y), \quad (5.2b)$$

with A being the amplitude and U_0 an integral constant. In summary, therefore, in the streamwise-rotating channel, the condition (3.11), which permits the inertial-wave solutions, implies that the streamwise and spanwise mean-velocity profiles take the cosine and sine forms, respectively.

To verify whether the IW condition is achieved in our flow, we use DNS data to calculate the cosine of the angle spanned by $\partial_y \boldsymbol{\Omega}$ and $\partial_y \mathbf{U}$

$$\cos \alpha(y) = \frac{\partial_y \boldsymbol{\Omega}(y) \cdot \partial_y \mathbf{U}(y)}{|\partial_y \boldsymbol{\Omega}(y)| |\partial_y \mathbf{U}(y)|}. \quad (5.3)$$

The variations of $\cos \alpha$ as y are shown in figure 11(a) for all four cases. Clearly, except for Case ST05, over a certain range at the centre region there is $\cos \alpha \approx -1$. This implies that not only for three cases with larger Ro the mean flows at the central region do satisfy the IW condition, but also $\partial_y \boldsymbol{\Omega}$ and $\partial_y \mathbf{U}$ have the opposite directions in this region. Thus, the inertial-wave solutions should have $s = -1$, which matches the fact revealed by HWD that the $s = -1$ modes overwhelm the ones with $s = +1$. Besides, the IW condition (3.11) also fixes the wavenumber K_{in} of the inertial waves, as given by (3.15), of which the calculated values by the mean-flow profiles of DNS data are shown in figure 11(b). Except for Case ST05, K_{in} is basically around 5 in the

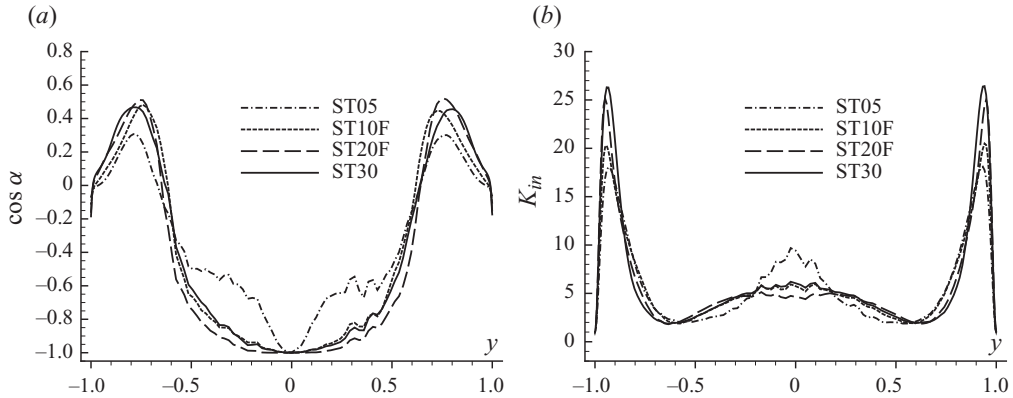


FIGURE 11. (a) $\cos \alpha$ defined in (5.3) and (b) K_{in} in (3.15) calculated with the mean-flow quantities obtained by DNS.

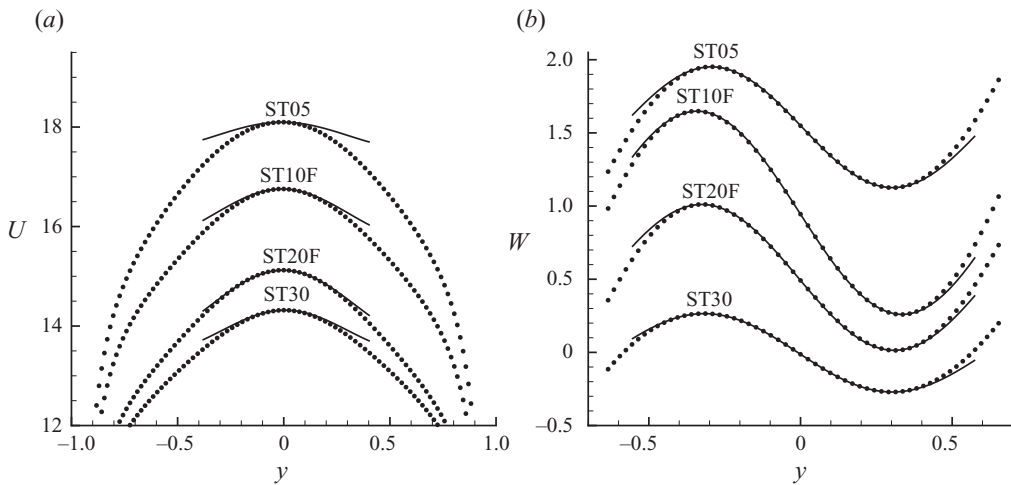


FIGURE 12. The comparison of the theoretical predictions (5.2a) and (5.2b) and mean-flow profiles obtained by DNS. Lines, fitting curves; symbols, DNS results. (a) The curves are shifted upwards from the previous one by 0.5.

region where $\cos \alpha \approx -1$. This K_{in} value is in agreement with the wavenumber K_m with the highest energy, as shown by the helical spectra in figure 6.

In figure 11(b) the K_{in} curves are rather fluctuating at the centre of the channel, where the computing meshes are coarsest through the channel span. In order to determine the value of K_{in} more precisely, we use the theoretical prediction (5.2b) to fit the W profiles given by the DNS, namely we determine the locations and values of the two inboard peaks and the zero points of the W curves in figure 2(b), and identify the distance between the two peaks as the half of K_{in} . The values of K_{in} found thereby are listed in table 1. The peak value gives the amplitude A in (5.2b). In figure 12 the fitting curves are compared with the DNS results for several cases. Clearly, between the two inboard peaks, the theoretical prediction (5.2b) is perfectly verified by the numerical result for all the cases, which further confirms that the reverse spanwise flow is related to the inertial waves. For the streamwise mean flow, however, only in a much smaller neighbourhood of the centreline does the theoretical prediction (5.2a)

have reasonable accuracy (see figure 12a). The reason is that the mean-flow profile of the latter is also affected by the external mean pressure gradient, while the former mean profile is solely determined by the Reynolds stress produced by the fluctuating flow, mainly from inertial waves.

The preceding discussion reveals that the inertial waves permitted by the mean flow are exactly the most energetic helical modes found by HWD. They have the comparable wavenumber $k \approx K_{in} \approx K_m$ and the same polarity $s = -1$. The reason why K_{in} takes a similar value for different rotation numbers and domain sizes remains unclear. One may speculate that this value is related to the global characteristic length of the channel, i.e. the half-height h , which is the same for all cases. One supporting example is that in an enclosed cylindrical domain rotating about its axis the natural frequencies and the wavenumbers of the small inertial oscillation are determined by the rotating speed and the geometry of the cylinder, i.e. the radius and height (see Batchelor 1967).

Now, the discrepancy between the numerical and experimental results reported by Recktenwald *et al.* (2007, 2009) may be explained as follows. In the numerical simulations with periodic boundary condition, the flow periodicity permits the inertial waves to travel infinitely. In experiment with a finite-length channel, however, the inertial waves will quickly reach the boundary, which imposes new constraints on the existence of the inertial waves. Furthermore, Phillips (1963) has found that the inertial waves can be reflected at the wall and change the wavenumber after the reflection. These mechanisms make a dominant wavenumber unable to survive for a long time. Note that Recktenwald *et al.* (2009) abandoned the periodic condition in the spanwise direction but not in the streamwise direction. This can only affect the inertial waves whose wall-parallel wavenumbers have non-zero spanwise component. But still the inertial waves travelling in the streamwise direction may exist. This is likely why in Recktenwald *et al.* (2009) the mean profiles of LES did not match the experiments even for very large computational boxes. Note that the existence of inertial waves may also explain why all the streamwise two-point correlations approach a non-zero value rather than exactly zero, e.g. our figure 14 shown below, and the figures in Recktenwald *et al.* (2007) and Alkishriwi *et al.* (2008).

There remains one question to answer: why the mean profiles of Case ST05 do not satisfy the IW condition. In solving the inertial-wave solutions, we have made a strong assumption that the viscous term is negligible compared with the Coriolis force. By the fluctuating NS equation (4.6), a local ratio between the Coriolis force and viscous term, or a local Ekman number, can be defined as

$$\gamma(y) = (|2\mathbf{R} \times \mathbf{u}|/|\nu \nabla^2 \mathbf{u}|), \quad (5.4)$$

where $|\cdot|$ means the magnitude of the vector. The γ curves are shown in figure 13. The maxima of γ locate at the centreline and increase as system rotates faster. When $Ro = 5$, γ is below 5, while for all other three cases γ exceeds 10 at the centre region. Thus, for the rotation rates considered here, the inviscid assumption is reasonable for $Ro \geq 10$ such that the Coriolis force is larger than the viscous term by more than one order at the channel centre. The viscous effect in Case ST05 is too strong to ignore. A more accurate estimation of the critical Ro at which the viscous term is negligible needs more simulations in the range $Ro \in (5, 10)$. Another factor which may affect this critical value is the channel size, since figure 11(a) and figure 12 show that the mean velocity of Case ST20F satisfies the IW condition and the fitting law (5.2) over a wider region than that of ST30.

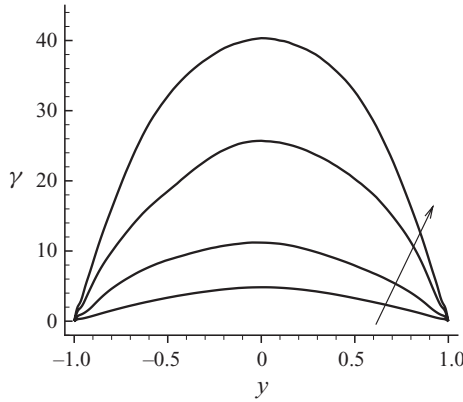


FIGURE 13. The ratio of the Coriolis force to the viscous term in the fluctuating momentum balance. The arrow indicates the increase of Ro from 5 to 30.

5.2. Long vortex clusters

Having shown that in the central part of the channel there may exist structures with large streamwise scales, which are very likely the carrier of inertial waves, we now identify these structures in the physical space.

Consider first the two-point correlation defined as

$$R(\mathbf{r}, y) = \frac{\overline{u(\mathbf{x}_\pi, y, t) u(\mathbf{x}_\pi + \mathbf{r}, y, t)}}{\overline{u^2(\mathbf{x}_\pi, y, t)}}, \quad (5.5)$$

where u is the streamwise component of the fluctuating velocity, $\mathbf{x}_\pi = x\mathbf{e}_x + z\mathbf{e}_z$ is the wall-parallel component of the location vector and $\mathbf{r} = r_x\mathbf{e}_x + r_z\mathbf{e}_z$ is the displacement vector in a wall-parallel plane between two points. Two different correlations have been computed: the streamwise two-point correlation $R_1(r_x, y)$ with $\mathbf{r} = r_x\mathbf{e}_x$ and the spanwise two-point correlation $R_2(r_z, y)$ with $\mathbf{r} = r_z\mathbf{e}_z$. These two functions reveal the coherent length scales in two directions.

Figure 14 shows the contours of R_1 and R_2 in the (r_x, y) and (r_z, y) planes for Case ST30, respectively. In the streamwise direction, the central region of the channel has larger correlation than the near-wall region. Two parallel ridges with higher correlation appear in the R_1 contours and locate symmetrically at two sides of the channel centreline. Due to these ridges, R_1 does not approach to zero when r_x reaches the half-length of the channel, thus the corresponding structures extend over the whole channel length. Furthermore, these ridges are at around $y = \pm 0.35$, and coincide with the locations of the inboard peaks in the W profile (see figure 2b). This observation confirms our previous statement that the reverse spanwise mean flow is associated with the structures of large streamwise scale.

For the spanwise correlation R_2 shown in figure 14(b), the correlation scales are rather small compared to R_1 . As r_z grows from zero, R_2 quickly reaches its minima at $r_z \approx 1$. The two negative peaks locate at $y \approx \pm 0.5$, which are closer to the wall than the ridges in R_1 contours. The positive and negative peaks appear alternately for several times when r_z becomes even larger, indicating that the flow structures are repeated rather regularly in the spanwise direction.

Two correlation functions indicate that similar structures appear simultaneously at both sides of the centreline and have very long streamwise scales and relatively small spanwise scales. We employ the λ_2 criteria proposed by Jeong & Hussain (1995) to

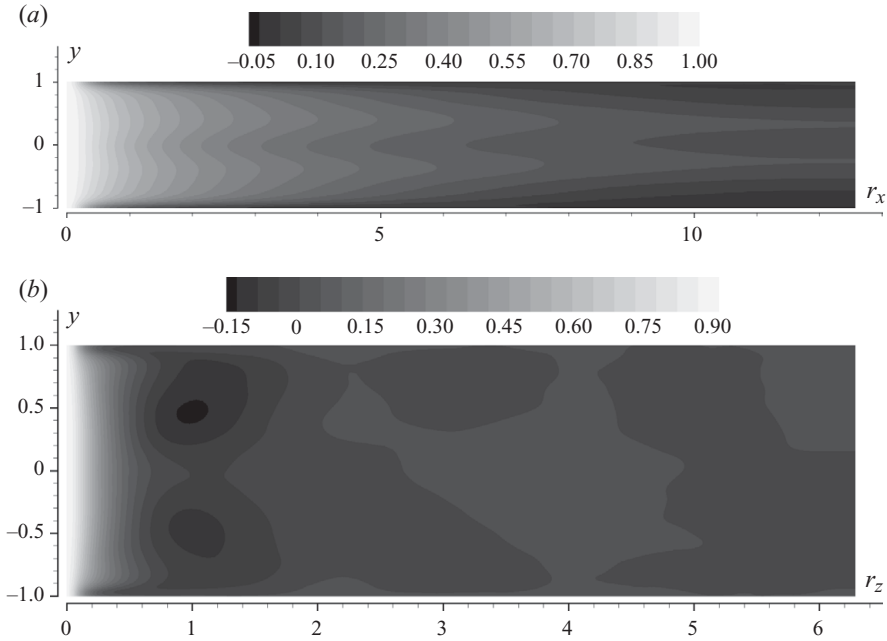


FIGURE 14. The contours of (a) the streamwise two-point correlation $R_1(r_x, y)$ and (b) the spanwise two-point correlation $R_2(r_z, y)$ for Case ST30.

visualize these vortical structures. Figure 15 shows an iso-surface of λ_2 for Case ST30 at the central region of the channel within the layer $-0.7 < y < 0.7$. The layer consists of two parts, above and below the centreline, which are shown separately. It is obvious that the small vortical structures are clustered and form very long columns. In each layer, these columns have almost the same direction and make a small angle away from the direction of the rotation axis. In the upper layer, the columns are inclined to the positive z direction (see figure 15a), and *vice versa* in the lower layer shown in figure 15(b). The orientation of the columns, either above or below the centreline, coincides with the directions of the outboard peaks of W profile in figure 2(b).

Further observation on a series of instantaneous fields (not shown here) at sequential time steps indicates that the inclined columns in figure 15 move to the right in the (x, z) plane. Thus, for an observer at a fixed location in these regions, the passing flow has a wave-like vorticity variation, which should be the material carrier of the inertial waves. Similar twisted travelling waves have also been found in the instability analysis of Masuda *et al.* (2008), where the Reynolds number is much smaller than that of the present study.

In figure 15, we also show the contours of the fluctuating streamwise velocity at two (x, z) planes with a distance $y^+ = 10$ to the corresponding wall. Clearly, the vortex columns at the centre region of the channel locate just above the low-speed streaks near the walls. It is well known that these low-speed streaks are related to the creation of the streamwise vortices. Now, a possible scenario can be proposed. Near the lower wall, for instance, the system rotation induces a negative spanwise velocity, as shown in figure 2(b), which causes the low-speed streaks twisting to the negative z direction (see the background contours in figure 15b). Thus, the accompanying near-wall streamwise vortices will also incline to the same direction. Then the twisted-streamwise vortices are lifted to the core region of the channel, where the viscous

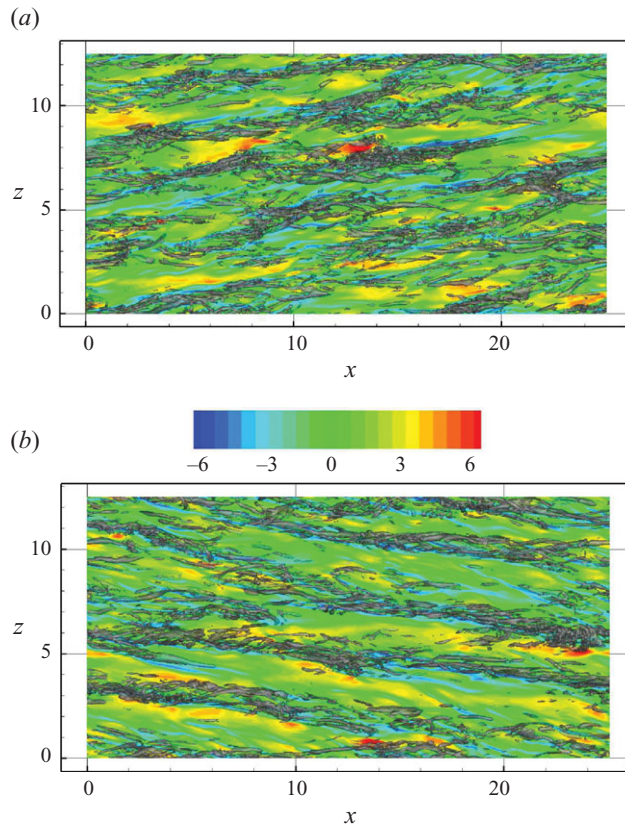


FIGURE 15. Top view of the vortical structures in the central part of the channel, which are illustrated by an iso-surface of λ_2 for Case ST30. The background contours are the fluctuating streamwise velocity u on the $y^+ = 10$ planes away from the corresponding walls. (a) $0 < y < 0.7$; (b) $0.7 < y < 1.0$.

effects are relatively small. Under the influence of the background rotation, the vortices form long columns as in the homogeneous rotating case, instead of evolving freely as in the non-rotating channel. The inclined vortex columns then travel downstream under the external mean pressure gradient in the streamwise direction. Because the columns are not parallel to the rotating axis and the direction of the mean pressure gradient, it will cause a transverse group velocity in the spanwise direction.

In the homogeneous rotating turbulence, the flow exhibits the quasi-two-dimensional columnar structures that show the cyclone/anticyclone-asymmetry. This has been confirmed by both the numerical simulations of Bartello, Métais & Lesieur (1994), Smith & Lee (2005) and Bourouiba & Bartello (2007), and the experiments of Morize, Moisy & Rabaud (2005), Staplehurst, Davidson & Dalziel (2008) and Moisy *et al.* (2010), to name a few. By using the method in those literatures, we may now examine the analogy of the twisted clusters in a streamwise-rotating channel to the phenomena in the homogeneous rotating turbulence. Specifically, the skewness of the total streamwise vorticity is computed at every wall-parallel plane as

$$S(y) = \overline{\omega_x^3} / (\overline{\omega_x^2})^{3/2}, \quad (5.6)$$

which is plotted in figure 16 for four rotating rates and compared with the non-rotating case. For a streamwise-rotating channel, S is negative around the centreline

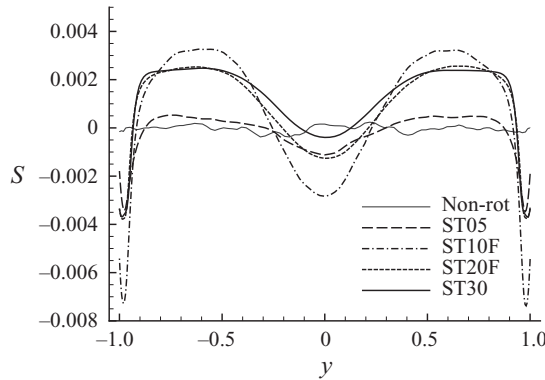


FIGURE 16. The skewness $S(y)$ for four rotating cases and the non-rotating case.

and in the near-wall regions. In between, S takes a small positive value for $Ro \geq 10$, which implies a weak preference for the cyclone streamwise vorticity (in the same direction as \mathbf{R}), similar to the homogeneous case. Again, a non-monotonic behaviour appears as Ro increases. Bourouiba & Bartello (2007) have revealed that in decaying turbulence the skewness reaches a maximum at some intermediate Rossby number, and then decreases for higher rotating rate. Thus, there exists a certain analogy between the rotating channel and decaying turbulence on the cyclone/anticyclone-asymmetry, though the domain size may still have some effects on the skewness.

We have also tried to estimate the group velocity of the vortex columns by computing the two-time-two-point correlation of the streamwise vorticity ω_x for a fixed time separation Δt , which is given by

$$R(\mathbf{r}, y) = \overline{\omega_x(\mathbf{x}_\pi, y, t) \omega_x(\mathbf{x}_\pi + \mathbf{r}, y, t + \Delta t)}. \quad (5.7)$$

Two such correlations were calculated, which are R_3 with $\mathbf{r} = r_x \mathbf{e}_x$ and R_4 with $\mathbf{r} = r_z \mathbf{e}_z$, respectively. The Δt for R_3 is 0.1. For R_4 we choose a bigger time separation $\Delta t = 0.2$ because the spanwise group velocity is relatively small. The value of r_x (or r_z) where the correlation reaches the first maximum should measure the distance travelled by the fluctuating quantity over time duration Δt , which determines the group velocity.

In figure 17, we plot the typical contours of R_3 and R_4 for Case ST30. The streamwise group velocity is positive for $-0.7 < y < 0.7$. Around the centreline, the R_3 maxima locates at about $r_x \approx 1.5$, which gives $c_{gx} \approx 15$. The R_4 contours show that the group velocity is positive below the centreline and negative above the centreline. They are consistent with the direction of the reverse spanwise flow. The magnitude of c_{gz} at $y = \pm 0.3$ is approximately $0.2/0.2 = 1$, which is larger than the mean spanwise velocity $W \approx 0.45$. Unfortunately, the error for the group velocity estimated by this method depends strongly on the mesh size and the time separation as $dx/\Delta t$ or $dz/\Delta t$. For the grids used in ST30 and Δt we chose the errors for c_{gx} and c_{gz} to be about 0.98 and 0.25, respectively, too large to make good quantitative sense. Increasing Δt can reduce the error but the correlation will decrease, which will cause inaccuracy in locating the peaks. Thus, finer meshes are needed to calculate the accurate group velocity and validate the relation (3.14).

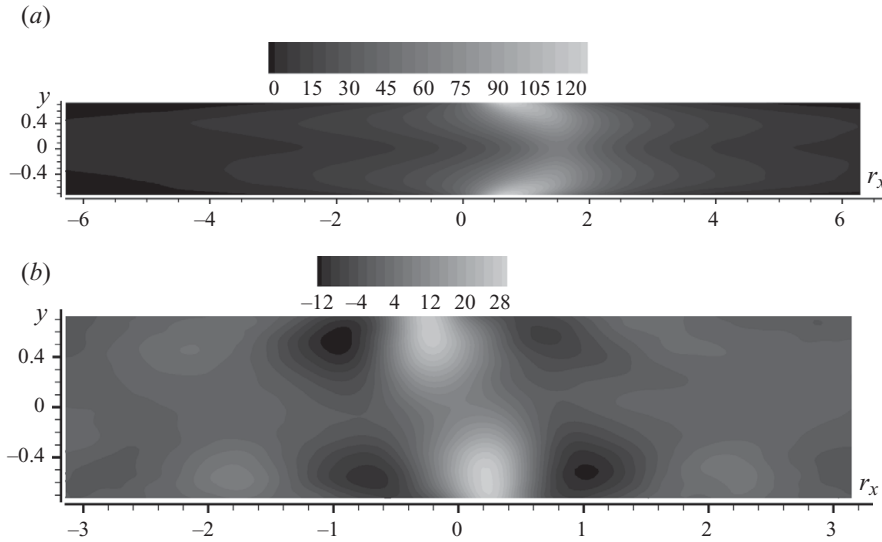


FIGURE 17. The contours of the two-time-two-point correlations $R_3(r_x, y)$ and $R_4(r_z, y)$ for Case ST30 in the region $-0.7 < y < 0.7$.

6. Conclusions

Although it has long been known that HWD is available for bounded domains and has great advantages in the studies of flows with system rotation, most of the existing works have been confined to the periodic or infinite domain for simplicity. In this paper, we first review the general formulation of HWD for an arbitrary single-connected domain. We show that for the incompressible flow with no-slip boundary, an extra boundary integral appears in the dynamic equation of a single helical mode, since the vorticity usually has non-zero wall-parallel component on the no-slip boundary. In order to apply the theory to channel flow, we solve the helical bases for this model domain. The bases can then be used to decompose the flow field into helical modes with different scales and polarities.

For the channel rotating about an axis parallel to the walls, we derive the HWD of the Coriolis force and prove that this term does not affect the energy contained in a single helical mode. Meanwhile, the helical basis functions are employed to construct the inertial-wave solutions in a channel domain. Theoretical results reveal that when the channel has a basic mean flow, the inertial waves still exist if the mean flow satisfies an IW condition. The mean flow also determines the polarity and wavenumber of the inertial waves and other properties, such as the frequency, phase and group velocities.

To demonstrate the theory, we perform the DNS of the channel flow with streamwise rotation and the numerical HWD of the flow fields. The helical energy spectra for different rotating rates indicate that the streamwise rotation breaks the symmetry between two opposite polarities. The negative polarity carries more energy than the positive one. The energy concentrates to a particular wavenumber, which is the same for all the rotating rates considered here. These observations imply that some dominant structures of certain scales appear in the flow.

Studies have suggested that in a streamwise-rotating channel the reverse mean flow in the spanwise direction is related to some large-scale structures in the core region. We verify the IW condition by the mean flow obtained from DNS data. The results show that the condition is indeed satisfied in the core region, and the profiles

of the mean flow match the theoretical predictions perfectly, which confirms the existence of the inertial waves. The wavenumber of the inertial waves determined by the mean flow coincides with that of the most energetic modes in the helical spectra, suggesting that the waves are associated with some strong coherent structures. By the flow visualization, we show that these structures are very long vortex columns in the central region of the channel, which make a small angle away from the streamwise direction, i.e. the direction of the rotating axis. These vortex columns, which move downstream in the wall-parallel plane, are very likely the carrier of the inertial waves.

This study introduces some new questions to both numerical simulation and experiment. In order to quantitatively clarify the relation between the vortex columns and the inertial waves, one needs to conduct DNS with much finer meshes to calculate the accurate group velocity. To detect the inertial waves experimentally, the configuration of the channel should be chosen very carefully, since the boundary introduces an extra constraint for the inertial waves to survive. Successful measurement of the inertial waves has been done for the rotating tank by Bewley *et al.* (2007). Another interesting subject is the non-monotonic behaviour of the flow statistics as Ro increases. Similar behaviour has been shown in decaying turbulence by Bourouiba & Bartello (2007). To clarify the non-monotonicity, the effects of the domain size should be studied thoroughly. Also, the underlying mechanism of the scaling laws exhibited by the helical spectra is of great interest. More simulations with higher Ro and Re are needed to clarify those issues.

The authors acknowledge the very inspiring discussion with Professor F. Hussain and the valuable comments of the referees. This work was supported in part by the National Natural Science Foundation of China (Key Project No. 10532010). The numerical simulations are conducted on the HP cluster at the Center of Computational Science and Engineering at Peking University.

Appendix A. The helical bases for a channel domain

The helical bases depend only on the geometric property of the domain; for each specific domain, they can be calculated once for all. For some simple domains, the bases may be derived analytically. Morse & Feshbach (1953) gave a general formula of the helical bases for the domain with rectangular, cylindrical, spherical or conical shape. A similar formula was obtained later by Chandrasekhar & Kendall (1957), which has been used by Morse (2005, 2007) to calculate the bases for a cylindrical domain and finite-length rectangular boxes. For even more complex geometries, the bases can be found numerically, e.g. the finite-volume algorithm of Boulmezaoud & Amari (2000).

Here, we briefly describe the derivation of the helical bases for the channel domain $(x, y, z) \in [0, L_x] \times [-h, h] \times [0, L_z]$. The periodic condition is employed at two homogeneous directions. We use the formula given by Chandrasekhar & Kendall (1957),

$$\phi_s = \nabla\psi \times \mathbf{e} + \frac{s}{k}[ek^2\psi + (\mathbf{e} \cdot \nabla)\nabla\psi], \quad (\text{A } 1)$$

where \mathbf{e} is one of the Cartesian unit vectors, and the scalar ψ satisfies the Helmholtz equation,

$$\nabla^2\psi + k^2\psi = 0. \quad (\text{A } 2)$$

The boundary condition for ψ is determined by ensuring $\mathbf{n} \cdot \phi_s = 0$ at two walls.

After the separation of variables, one finds out that the wavenumber can be written in vector form as

$$\mathbf{k} = (k_x, k_y, k_z) = \left(\frac{2\pi m}{L_x}, \frac{l\pi}{2h}, \frac{2\pi n}{L_z} \right), \quad (\text{A } 3)$$

with integers $m, n = 0, \pm 1, \pm 2, \dots$, and $l = 0, 1, 2, \dots$. The complete basis set is given as follows.

(a) When $m = n = 0$ and $l = 0, 1, 2, 3, \dots$

$$\phi = \Pi[0, 0, 1] \quad \text{for } l = 0, \quad (\text{A } 4a)$$

$$\phi_s = \Pi[s \cos(k_y y), 0, \sin(k_y y)] \quad l \text{ is odd}, \quad (\text{A } 4b)$$

$$\phi_s = \Pi[s \sin(k_y y), 0, -\cos(k_y y)] \quad l \text{ is even}. \quad (\text{A } 4c)$$

(b) When $m, n = 0, \pm 1, \pm 2, \dots$, with $m^2 + n^2 \neq 0$, and $l = 1, 2, 3, \dots$, then for odd l ,

$$\phi_s(\mathbf{k}, \mathbf{x}) = \frac{\Pi}{k} \begin{pmatrix} -i\sqrt{k_y^2 + k_z^2} \cos(k_y y - s\alpha) \\ s\sqrt{k_x^2 + k_z^2} \cos(k_y y) \\ i\sqrt{k_x^2 + k_z^2} \cos(k_y y + s\beta) \end{pmatrix} \exp[i(k_x x + k_z z)], \quad (\text{A } 5a)$$

and for even l ,

$$\phi_s(\mathbf{k}, \mathbf{x}) = \frac{\Pi}{k} \begin{pmatrix} -i\sqrt{k_y^2 + k_z^2} \sin(k_y y - s\alpha) \\ s\sqrt{k_x^2 + k_z^2} \sin(k_y y) \\ i\sqrt{k_x^2 + k_z^2} \sin(k_y y + s\beta) \end{pmatrix} \exp[i(k_x x + k_z z)]. \quad (\text{A } 5b)$$

Here, $k = |\mathbf{k}|$ and i is the imaginary unit. The constant and two phase angles are, respectively,

$$\Pi = \frac{1}{\sqrt{2hL_xL_z}}, \quad \tan \alpha = \frac{k_x k_y}{k k_z}, \quad \tan \beta = \frac{k_y k_z}{k k_x}.$$

The helical bases (A 5) have helix-like streamlines as in the periodic domain. Wavenumber vector \mathbf{k} determines the direction and geometric properties of helices, such as pitch length and diameter. Positive (negative) s corresponds to clockwise (anticlockwise) rotation when one moves along the helix-like streamlines. More details of the bases are reported in Yang (2009).

Appendix B. The inertial waves in channel without basic flow

Consider the channel with zero mean flow, i.e. $\mathbf{U} = \boldsymbol{\Omega} = \mathbf{0}$. The inviscid vorticity equation reads

$$\frac{\partial \boldsymbol{\omega}}{\partial t} + \nabla \times (\boldsymbol{\omega} \times \mathbf{u}) = 2\mathbf{R} \cdot \nabla \mathbf{u}. \quad (\text{B } 1)$$

Suppose (B 1) has the wave solution (3.9). Substituting (3.9) into (B 1) one finds the following dispersion relation:

$$f_s = -2s \frac{\mathbf{R} \cdot \mathbf{k}_\pi}{k} = -2s \mathbf{R} \cdot \boldsymbol{\kappa}, \quad (\text{B } 2)$$

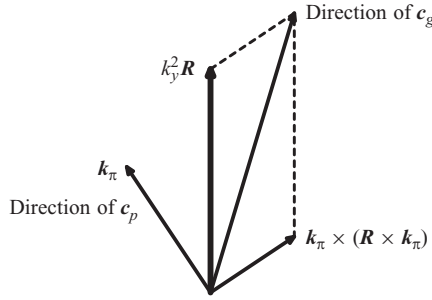


FIGURE 18. A sketch of the directions of \mathbf{R} , \mathbf{c}_p and \mathbf{c}_g for $s = -1$ for the zero-mean-flow case.

where $\boldsymbol{\kappa} = \mathbf{k}/k$ and the last equality is because \mathbf{R} has zero normal component. This dispersion relation has the same form as in the homogeneous case (see Greenspan 1969). The phase and group velocities are, respectively,

$$\mathbf{c}_p = -\frac{2s\mathbf{R} \cdot \boldsymbol{\kappa}}{|\mathbf{k}_\pi|^2} \mathbf{k}_\pi, \quad (\text{B } 3)$$

$$\mathbf{c}_g = -\frac{2s}{k^3} [k_y^2 \mathbf{R} + \mathbf{k}_\pi \times (\mathbf{R} \times \mathbf{k}_\pi)]. \quad (\text{B } 4)$$

Thus, \mathbf{c}_p is along \mathbf{k}_π in the wall-parallel plane, instead of \mathbf{k} as in the homogeneous domain. In the wall-normal direction, only standing waves with wavenumber k_y exist due to the constraint of the two walls. The short waves with large $|\mathbf{k}_\pi|$ travel slower than long waves with small $|\mathbf{k}_\pi|$. In figure 18, a sketch plot is shown to illustrate the relative directions of \mathbf{R} , \mathbf{c}_p and \mathbf{c}_g for negative polarity $s = -1$. For positive polarity $s = 1$, \mathbf{c}_p and \mathbf{c}_g take the opposite directions to that in figure 18.

Greenspan (1969) showed that in an infinite domain \mathbf{c}_g is along $\mathbf{k} \times (\mathbf{R} \times \mathbf{k})$ and orthogonal to \mathbf{c}_p at the right side. When $\mathbf{k} \parallel \mathbf{R}$, i.e. the wave travels along the rotation axis, one has $\mathbf{c}_g = \mathbf{0}$. But for the channel domain with no mean flow, the group velocity \mathbf{c}_g turns from the direction of $\mathbf{k}_\pi \times (\mathbf{R} \times \mathbf{k}_\pi)$ towards \mathbf{R} . When \mathbf{k}_π and \mathbf{R} are parallel to each other, \mathbf{c}_p and \mathbf{c}_g will have the same direction as the rotating axis \mathbf{R} .

REFERENCES

- ALKISHRIWI, N., MEINKE, M. & SCHRÖDER, M. 2008 Large-eddy simulation of streamwise-rotating turbulent channel flow. *Comput. Fluids* **37** (7), 786–792.
- BARTELLO, P., MÉTAIS, O. & LESIEUR, M. 1994 Coherent structures in rotating three-dimensional turbulence. *J. Fluid Mech.* **273**, 1–29.
- BATCHELOR, G. K. 1967 *An Introduction to Fluid Dynamics*. Cambridge University Press.
- BELLET, F., GODEFERD, F. S., SCOTT, J. F. & CAMBON, C. 2006 Wave turbulence in rapidly rotating flows. *J. Fluid Mech.* **562**, 83–121.
- BEWLEY, G. P., LATHROP, D. P., MAAS, L. R. M. & SREENIVASAN, K. R. 2007 Inertial waves in rotating grid turbulence. *Phys. Fluids* **19** (7), 071701.
- BOULMEZAOU, T. Z. & AMARI, T. 2000 Approximation of linear force-free fields in bounded 3-D domains. *Math. Comput. Modelling* **31** (2–3), 109–129.
- BOUROUBA, L. 2008 Model of a truncated fast rotating flow at infinite Reynolds number. *Phys. Fluids* **20**, 075112.
- BOUROUBA, L. & BARTELLO, P. 2007 The intermediate Rossby number range and two-dimensional–three-dimensional transfers in rotating decaying homogeneous turbulence. *J. Fluid Mech.* **587**, 139–161.
- CHANDRASEKHAR, S. & KENDALL, P. C. 1957 On force-free magnetic fields. *Astrophys. J.* **126**, 457–460.

- CHEN, Q. N., CHEN, S. Y. & EYINK, G. L. 2003 The joint cascade of energy and helicity in three-dimensional turbulence. *Phys. Fluids* **15** (2), 361–374.
- CHEN, Q. N., CHEN, S. Y., EYINK, G. L. & HOLM, D. D. 2005 Resonant interactions in rotating homogeneous three-dimensional turbulence. *J. Fluid Mech.* **542**, 139–164.
- DAVIDSON, P. A., STAPLEHURST, P. J. & DALZIEL, S. B. 2006 On the evolution of eddies in a rapidly rotating system. *J. Fluid Mech.* **557**, 135–144.
- DITLEVSEN, P. D. & GIULIANI, P. 2001a Cascades in helical turbulence. *Phys. Rev. E* **63** (3), 036304.
- DITLEVSEN, P. D. & GIULIANI, P. 2001b Dissipation in helical turbulence. *Phys. Fluids* **13** (11), 3508–3509.
- GREENSPAN, H. P. 1969 *The Theory of Rotating Fluids*. Cambridge University Press.
- GRUNDESTAM, O., WALLIN, S. & JOHANSSON, A. V. 2008 Direct numerical simulations of rotating turbulent channel flow. *J. Fluid Mech.* **598**, 177–199.
- JEONG, J. & HUSSAIN, F. 1995 On the identification of a vortex. *J. Fluid Mech.* **285**, 69–94.
- JOHNSTON, J. P., HALLEEN, R. M. & LEZIUS, D. K. 1972 Effects of spanwise rotation on the structure of two-dimensional fully developed turbulent channel flow. *J. Fluid Mech.* **56**, 533–557.
- KELLEY, D. H., TRIANA, S. A., ZIMMERMAN, D. S. & LATHROP, D. P. 2010 Selection of inertial modes in spherical Couette flow. *Phys. Rev. E* **81** (2), 026311.
- KIM, J., MOIN, P. & MOSER, R. 1987 Turbulence statistics in fully-developed channel flow at low Reynolds number. *J. Fluid Mech.* **177**, 133–166.
- KRAICHNAN, R. H. 1973 Helical turbulence and absolute equilibrium. *J. Fluid Mech.* **59**, 745–752.
- KRISTOFFERSEN, R. & ANDERSSON, H. 1993 Direct simulations of low-Reynolds-number turbulent flow in a rotating channel. *J. Fluid Mech.* **256**, 163–197.
- MAAS, L. R. M. 2003 On the amphidromic structure of inertial waves in a rectangular parallelepiped. *Fluid Dyn. Res.* **33** (4), 373–401.
- MASUDA, S., FUKUDA, S. & NAGATA, M. 2008 Instabilities of plane Poiseuille flow with a streamwise system rotation. *J. Fluid Mech.* **603**, 189–206.
- MELANDER, M. V. & HUSSAIN, F. 1993a Coupling between a coherent structure and fine-scale turbulence. *Phys. Rev. E* **48** (4), 2669–2689.
- MELANDER, M. V. & HUSSAIN, F. 1993b Polarized vorticity dynamics on a vortex column. *Phys. Fluids A* **5** (8), 1992–2003.
- MININNI, P. D., ALEXAKIS, A. & POUQUET, A. 2009 Scale interactions and scaling laws in rotating flows at moderate Rossby numbers and large Reynolds numbers. *Phys. Fluids* **21** (1), 015108.
- MININNI, P. D. & MONTGOMERY, D. C. 2006 Magnetohydrodynamic activity inside a sphere. *Phys. Fluids* **18** (11), 116602.
- MININNI, P. D., MONTGOMERY, D. C. & TURNER, L. 2007 Hydrodynamic and magnetohydrodynamic computations inside a rotating sphere. *New J. Phys.* **9** (8), 303.
- MOISY, F., MORIZE, C., RABAUD, M. & SOMMERIA, J. 2010 Anisotropy and cyclone-anticyclone asymmetry in decaying rotating turbulence. *J. Fluid Mech.* (in press). Accessible at: <http://arxiv.org/abs/0909.2599>, doi:10.1017/S0022112010003733
- MORIZE, C., MOISY, F. & RABAUD, M. 2005 Decaying grid-generated turbulence in a rotating tank. *Phys. Fluids* **17** (9), 095105.
- MORSE, E. C. 2005 Eigenfunctions of the curl in cylindrical geometry. *J. Math. Phys.* **46** (11), 113511.
- MORSE, E. C. 2007 Eigenfunctions of the curl in annular cylindrical and rectangular geometry. *J. Math. Phys.* **48** (8), 083504.
- MORSE, P. M. & FESHBACH, H. 1953 *Methods of Theoretical Physics*. McGraw-Hill.
- NAKABAYASHI, K. & KITOH, O. 1996 Low Reynolds number fully developed two-dimensional turbulent channel flow with system rotation. *J. Fluid Mech.* **315**, 1–29.
- NAKABAYASHI, K. & KITOH, O. 2005 Turbulence characteristics of two-dimensional channel flow with system rotation. *J. Fluid Mech.* **528**, 355–377.
- OBERLACK, M., CABOT, W., PETTERSSON REIF, B. A. & WELLER, T. 2006 Group analysis, direct numerical simulation and modelling of a turbulent channel flow with streamwise rotation. *J. Fluid Mech.* **562**, 383–403.
- ORLANDI, P. & FATICA, M. 1997 Direct simulations of turbulent flow in a pipe rotating about its axis. *J. Fluid Mech.* **343**, 43–72.
- PHILLIPS, O. M. 1963 Energy transfer in rotating fluids by reflection of inertial waves. *Phys. Fluids* **6** (4), 513–520.

- RECKTENWALD, I., ALKISHRIWI, N. & SCHRÖDER, W. 2009 PIV–LES analysis of channel flow rotating about the streamwise axis. *Eur. J. Mech. B Fluids* **28** (5), 677–688.
- RECKTENWALD, I., WELLER, T., SCHRÖDER, W. & OBERLACK, M. 2007 Comparison of direct numerical simulations and particle-image velocimetry data of turbulent channel flow rotating about the streamwise axis. *Phys. Fluids* **19** (8), 085114.
- SHAN, X. W. & MONTGOMERY, D. 1994 Magneto-hydrodynamic stabilization through rotation. *Phys. Rev. Lett.* **73** (12), 1624–1627.
- SMITH, L. M. & LEE, Y. 2005 On near resonances and symmetry breaking in forced rotating flows at moderate Rossby number. *J. Fluid Mech.* **535**, 111–142.
- SMITH, L. M. & WALEFFE, F. 1999 Transfer of energy to two-dimensional large scales in forced, rotating three-dimensional turbulence. *Phys. Fluids* **11** (6), 1608–1622.
- STAPLEHURST, P. J., DAVIDSON, P. A. & DALZIEL, S. B. 2008 Structure formation in homogeneous freely decaying rotating turbulence. *J. Fluid Mech.* **598**, 81–105.
- THIELE, M. & MÜLLER, W. 2009 Structure and decay of rotating homogeneous turbulence. *J. Fluid Mech.* **637**, 425–442.
- TURNER, L. 1999 Macroscopic structures of inhomogeneous, Navier–Stokes turbulence. *Phys. Fluids* **11** (8), 2367–2380.
- TURNER, L. 2000 Using helicity to characterize homogeneous and inhomogeneous turbulent dynamics. *J. Fluid Mech.* **408**, 205–238.
- ULITSKY, M., CLARK, T. & TURNER, L. 1999 Testing a random phase approximation for bounded turbulent flow. *Phys. Rev. E* **59** (5), 5511–5522.
- WALEFFE, F. 1992 The nature of triad interactions in homogeneous turbulence. *Phys. Fluids A* **4** (2), 350–363.
- WALEFFE, F. 1993 Inertial transfers in the helical decomposition. *Phys. Fluids A* **5** (3), 677–685.
- WU, H. & KASAGI, N. 2004 Effects of arbitrary directional system rotation on turbulent channel flow. *Phys. Fluids* **16** (4), 979–990.
- WU, J. Z., MA, H. Y. & ZHOU, M. D. 2006 *Vorticity and Vortex Dynamics*. Springer.
- YANG, Y. T. 2009 Local dynamics and multi-scales interaction in complex shearing flows. PhD thesis, Peking University, Beijing, China (in Chinese).
- YEUNG, P. K. & ZHOU, Y. 1998 Numerical study of rotating turbulence with external forcing. *Phys. Fluids* **10** (11), 2895–2909.
- YOSHIDA, Z. & GIGA, Y. 1990 Remarks on spectra of operator rot. *Math. Z.* **204**, 235–245.